Application of a 2D harmonic polynomial cell (HPC) method to singular flows and lifting problems

Hui Liang[1, 2, *], Odd M. Faltinsen[1], Yan-Lin Shao[1, 3]

[1]: *Centre for Autonomous Marine Operations and Systems (AMOS), Department of Marine Technology, NTNU, NO-7491Trondheim, Norway.*

[2]: *School of Naval Architecture Engineering, State Key Laboratory of Structural Analysis for Industrial Equipment, Dalian University of Technology, Dalian 116024, People's Republic of China.*

[3]: *Sevan Marine ASA, 0277 Oslo, Norway.*

Abstract:

Further developments and applications of the 2D harmonic polynomial cell (HPC) method proposed by Shao and Faltinsen [22] are presented. First, a local potential flow solution coupled with the HPC method and based on the domain decomposition strategy is proposed to cope with singular potential flow characteristics at sharp corners fully submerged in a fluid. The results are verified by comparing them with the analytical added mass of a double-wedge in infinite fluid. The effect of the singular potential flow is not dominant for added mass and damping, but the error is non-negligible when calculating mean wave loads using direct pressure integration. Then, the double-layer nodes technique is used to simulate a thin free shear layer shed from lifting bodies, across which the velocity potential is discontinuous. The results are verified by comparing them with analytical results for steady and unsteady lifting problems of a flat plate in infinite fluid. The latter includes the Wagner problem and the Theodorsen functions. Satisfactory agreement with other numerical results is documented for steady linear flow past a foil and beneath the free surface.

Keywords: HPC; Marine hydrodynamics; Local solution; Domain decomposition; Double-layer nodes;

---

*Corresponding author. Email address: lianghuistar@gmail.com (Hui Liang)
Present address: Deepwater Technology Research Centre (DTRC), Bureau Veritas Marine (Singapore) Pte Ltd, Singapore 117674.

1 Introduction

Computational fluid dynamics (CFD) based on the Navier-Stokes (NS) equations and an incompressible fluid have played an increasingly important role in marine hydrodynamics. However, simulations of wave load effects in a stochastic sea are limited by the computational time associated with CFD. In contrast, a potential flow solver is more efficient than a typical NS solver. When the wave-induced responses of large-volume structures, such as ships and floating platforms, are considered, the viscous effect may only be significant near the body and typically affects resonance problems with small wave radiation damping. Thus, the domain decomposition strategy, which applies a NS solver in the region where the viscous effect dominates and solves the Laplace equation elsewhere, has been employed [12, 14].

Within the context of potential flow theory, the boundary element method (BEM) has been widely applied [8, 18]. Because the coefficient matrix for the unknowns is full, the computational time and memory required by the BEM increase strongly as the number of unknowns increases. Wu and Eatock Taylor [27] argue that a field-solver based on the finite element method (FEM) is faster than the BEM for solving the wave-making problem because a sparse matrix is involved in the solution. The conventional BEM involves quadratic memory usage, $O(N^2)$, and requires $O(N^2)$ operations for an iterative solver or $(O(N^3))$ operations if a direct method is used [28]. Here, N is the number of unknowns; thus, large-scale storage and inefficient computation are considered bottleneck problems in the conventional BEM. Recent studies have shown that these difficulties can be overcome by using accelerating techniques, such as the fast multipole accelerated (FMA) method [21, 15] and the pre-corrected fast Fourier transform (p-FFT) technique [29]. Consequently, FMA and p-FFT accelerated BEMs require $O(N)$ and $O(N\log N)$ operations to solve the boundary integral equation, respectively.

High-order methods have received increasing attention for obtaining high accuracy. Yan and Liu [29] developed the p-FFT high-order BEM to study nonlinear wave-body interaction problems. Bingham and Zhang [5] used a higher-order finite difference method (FDM) to model nonlinear water waves using potential flow theory.

Shao and Faltinsen [22] proposed a potential flow solver, the 2D harmonic polynomial cell (HPC) method, with an order greater than third order. When using this method, the liquid domain is divided into cells and harmonic polynomials, which satisfy the Laplace equation and are used to represent the velocity potential in each cell. The resulting equation system involves a sparse matrix, implying computational efficiency. Shao and Faltinsen [22] compared the HPC method with four other 2D Laplace equation solvers and found that the HPC method is highly efficient and the most accurate among the considered solvers. In addition, Faltinsen and Timokha [11] used harmonic polynomials to analytically study the 2D frequency-domain sloshing problem. Fredriksen et al. [12] combined the HPC method and a Navier-Stokes equation solver

employing the finite volume method (FVM) to investigate the piston-mode resonance in moonpools with a low forward speed by using domain decomposition and a 2D flow assumption. Recently, Shao and Faltinsen [23] conducted a comprehensive study of the 3D HPC method. In addition, fully nonlinear free-surface problems involving a numerical wave tank and wave interactions with a vertical free-surface piercing circular cylinder standing on the sea floor were investigated. The observed satisfactory agreement with these experiments and other numerical results indicates that the HPC method is an efficient, accurate and promising method for solving potential flow problems.

Although the HPC method has been used to solve a series of problems in marine hydrodynamics [22, 23], it is not ideal. The HPC method must be modified to handle singular flows and discontinuous problems within the framework of potential flow. One example is the corner flow problem of non-separated flow, in which the velocity components are singular at the apex when the interior angle is less than 180° [19]. A state-of-the-art BEM cannot account for flow singularities because piecewise polynomial representation of unknowns is assumed at boundaries. Another example is a thin free shear layer shed from a foil, where the velocity potential is discontinuous across the shear layer. To overcome these difficulties, several algorithms are proposed in this paper. The local potential flow solution coupled with the HPC method following the domain decomposition strategy is proposed to simulate the singularity at the apex of the corner, and a double-layer node technique is developed to model the shedding of a thin free shear layer from lifting bodies.

This paper is organized as follows. In Section 2, we present the basic formulations of the 2D HPC method and describe the linear frequency-domain analysis of free-surface flow. In Section 3, a domain decomposition strategy combining the local potential flow solution and the HPC method is proposed to address fluid-structure problems in the presence of sharp corners. Section 4 describes the double-layer nodes technique in the HPC method to model the effects of a thin free shear layer in which velocity potential jumps exist. In Section 5, extensive numerical examples are conducted, including an oscillating wedge in infinite fluid, the second-order mean vertical force on a heaving floating rectangular cylinder, steady and unsteady lifting problems in infinite fluid and the steady lifting problem for a NACA hydrofoil in the presence of a free surface. Finally, concluding remarks and future perspectives are presented in Section 6.

2 Summary of the 2D HPC method

2.1 Governing equation

An incompressible and inviscid fluid with irrotational 2D flow is assumed. The resulting velocity potential ϕ satisfies the Laplace equation as follows:

$$\frac{\partial^2 \phi}{\partial x^2} + \frac{\partial^2 \phi}{\partial y^2} = 0, \tag{1}$$

3

in the Cartesian coordinate system Oxy.

2.2 2D HPC method

The harmonic polynomials satisfy the Laplace equation and are based on the real and imaginary parts, $u_n(x, y)$ and $v_n(x, y)$, of the complex potential

$$(x+iy)^n = u_n(x, y) + iv_n(x, y),$$ (2)

where $i = \sqrt{-1}$ is the imaginary unit and n is an integer indicating the order of the harmonic polynomials. Table 1 depicts the harmonic polynomials for $n \leq 4$.

Table 1. Two-dimensional harmonic polynomials up to fourth-order.

n	$(x+iy)^n$	$u_n(x, y)$	$v_n(x, y)$
0	$(x+iy)^0$	1	0
1	$(x+iy)^1$	x	y
2	$(x+iy)^2$	$x^2 - y^2$	$2xy$
3	$(x+iy)^3$	$x^3 - 3xy^2$	$3x^2y - y^3$
4	$(x+iy)^4$	$x^4 - 6x^2y^2 + y^4$	$4x^3y - 4xy^3$

When considering a 2D fluid domain, we discretize the computational domain into a number of quadrilateral elements, as shown in Fig. 1 (a). In the present 2D HPC method, each stencil cell is defined as the combination of four neighboring quadrilateral elements with nine grid points, as demonstrated in Fig. 1 (a). The local index of grid points over the cell is defined in Fig. 1 (b), with the first eight grid nodes as boundary nodes and the ninth node as the stencil center. The velocity potential at each node is represented by the harmonic polynomials. Hence, the velocity potential in each cell naturally satisfies the Laplace equation.

According to [22], the velocity potential at any point within the cell can be approximated by a linear combination of the first eight harmonic polynomials, which takes the following form:

$$\phi(x, y) = \sum_{j=1}^{8} b_j f_j(x, y),$$ (3)

with

$$f_1(x, y) = 1; \quad f_2(x, y) = x; \quad f_3(x, y) = y; \quad f_4(x, y) = x^2 - y^2; \quad f_5(x, y) = xy;$$
$$f_6(x, y) = x^3 - 3xy^2; \quad f_7(x, y) = 3x^2y - y^3; \quad f_8(x, y) = x^4 - 6x^2y^2 + y^4.$$ (4)

In Eq. (3), ϕ denotes the velocity potential in the cell and f_j $(j = 1, ..., 8)$ represents the first eight nonzero harmonic polynomials defined in Table 1. In addition, b_j are unknown

coefficients that must be determined.

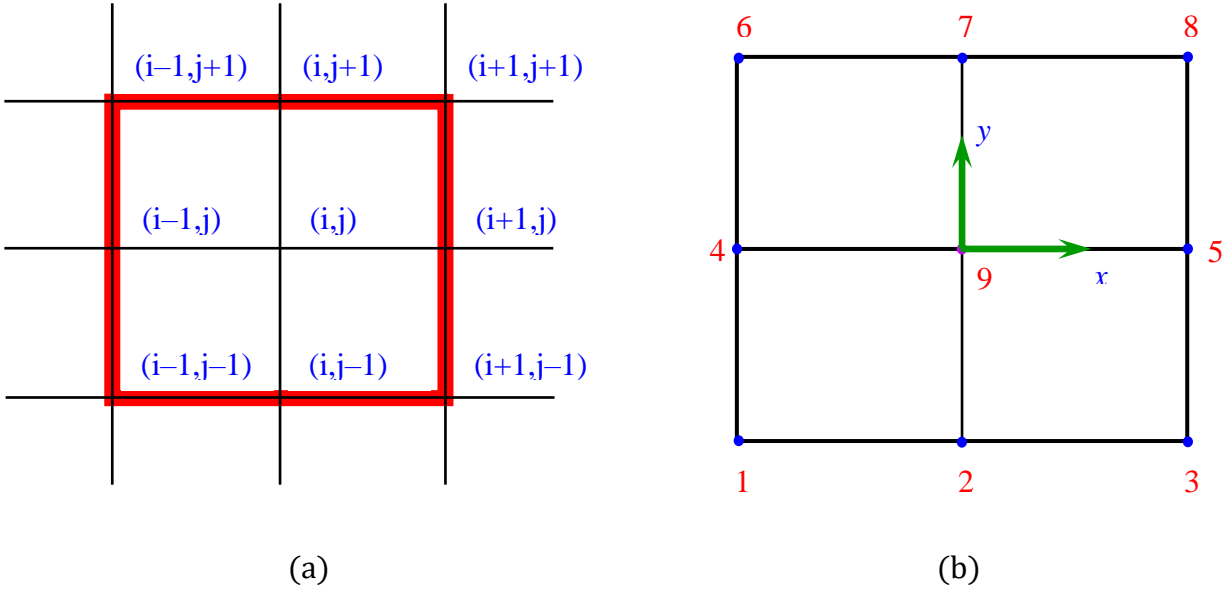(a)   (b)

Fig. 1 Global index and local index of the grid nodes in a cell.

By setting $x = x_j$, $y = y_j$ and $\phi = \phi_j$ $(j = 1, \dots, 8)$ in Eq. (3), we can obtain a linear equation system with the following form:

$$[\mathbf{A}] \cdot \{\mathbf{b}\} = \{\boldsymbol{\phi}\}, \tag{5}$$

where the elements in the coefficient matrix $[\mathbf{A}]$ are $a_{i,j} = f_j(x_i, y_i)$. Here i and j denote the row index and column index of the matrix $[\mathbf{A}]$, respectively. Eq. (5) can be rewritten in a concise form as follows:

$$b_i = \sum_{j=1}^{8} c_{i,j} \phi_j, \quad (i = 1, \dots, 8), \tag{6}$$

where $c_{i,j}$ $(i = 1, \dots, 8)$ is the inverse of the matrix $[\mathbf{A}]$.

Combining Eq. (3) and Eq. (6) yields the following:

$$\phi(x, y) = \sum_{i=1}^{8} \left[\sum_{j=1}^{8} c_{i,j} \phi_j \right] f_i(x, y)$$

$$= \sum_{i=1}^{8} \left[\sum_{j=1}^{8} c_{j,i} f_j(x, y) \right] \phi_i. \tag{7}$$

Eq. (7) indicates that the velocity potential at any point in the cell can be interpolated by the velocity potentials at the surrounding boundary nodes of the cell. By setting $x = x_9 = 0$ and $y = y_9 = 0$, the harmonic polynomials in Eq. (4) can be simplified to $f_j(0,0) = 1$ and $f_j(0,0) =$

0, where $j = 2, \ldots, 8$. Thus, according to Eq. (7), the velocity potential at local grid point 9 becomes:

$$\phi_9 = \phi\left(x = x_9 = 0, y = y_9 = 0\right) = \sum_{i=1}^{8} c_{1,i} \phi_i. \tag{8}$$

With respect to the Neumann condition, the normal derivative can be obtained by calculating the derivative of the harmonic polynomials, which takes the following form:

$$\frac{\partial \phi}{\partial n}(x, y) = \sum_{i=1}^{8} \left[\sum_{j=1}^{8} c_{j,i} \nabla f_j(x, y) \cdot \boldsymbol{n}(x, y) \right] \phi_i, \tag{9}$$

where $\boldsymbol{n}$ denotes the normal vector, which is positive and points to the outside of the considered fluid domain.

2.3 Linearized frequency-domain analysis

For the wave diffraction/radiation problem without forward speed, the linear free-surface boundary condition in the frequency domain is expressed as follows:

$$-\kappa\phi + \frac{\partial \phi}{\partial y} = 0 \quad \text{on} \quad y = 0, \tag{10}$$

with $\kappa = \omega^2/g$, where ω is the frequency of oscillation.
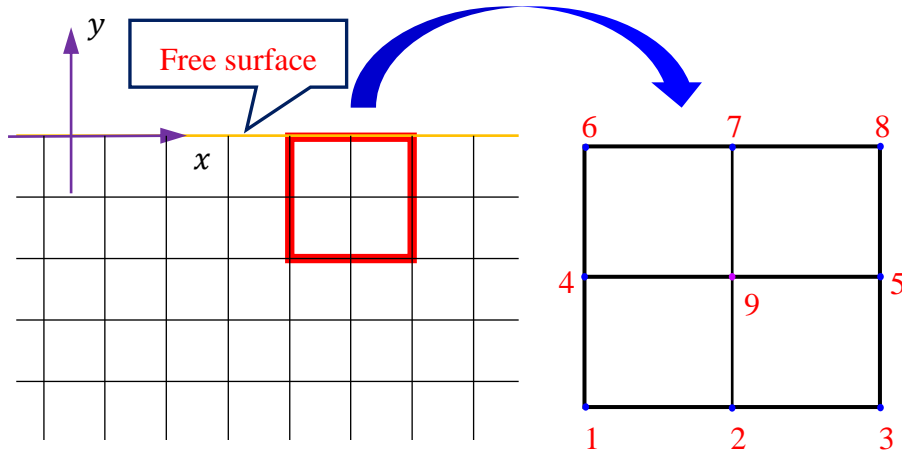

Fig. 2. Local index of the grid nodes in a cell attached to a free surface.

Eq. (9) provides the normal velocity expression of the boundary. If we consider the linearized frequency-domain free-surface condition given by (10) imposed on the undisturbed free surface, as illustrated in Fig. 2, the boundary condition should be satisfied at local node 7; thus, the boundary condition can be expressed as follows:

$$-\kappa\phi_7 + \sum_{i=1}^{8}\left[\sum_{j=1}^{8}c_{j,i}\frac{\partial}{\partial y}f_j(x_7,y_7)\right]\phi_i = 0 \quad \text{on} \quad y = 0. \tag{11}$$

3 Corner solution coupled with the HPC method

To demonstrate the singular characteristics of the corner flow within a potential flow, we consider the flow past a sharp corner with an included angle β and a corresponding interior angle of $\psi = 2\pi - \beta$, as shown in Fig. 3. The considered semi-infinite wedge is fixed, and the origin of the polar coordinate system $Or\theta$ coincides with the origin of the Cartesian coordinate Oxy in Fig. 3, with $\theta = 0$ corresponding to the $Ox-$axis. The velocity potential

$$\phi = A_j r^{j\pi/\beta}\cos\left(\frac{j\pi}{\beta}\theta\right) = A_j r^{\frac{j\pi}{2\pi-\psi}}\cos\left(\frac{j\pi}{2\pi-\psi}\theta\right) \tag{12}$$

satisfies the zero Neumann body boundary condition. Here, A_j is a constant and j can be zero or any negative or positive integer. We can exclude negative integers by requiring that the fluid velocity flux through a surface with radius a enclosing the corner and extending from $\theta = 0$ to β approaches zero as $a \to 0$. The velocity determined based on Eq. (12) is singular at the apex when $j = 1$ and $\psi < \pi = 180°$. The latter relationship cannot be described by harmonic polynomials, which assume that the velocity potential is analytical.
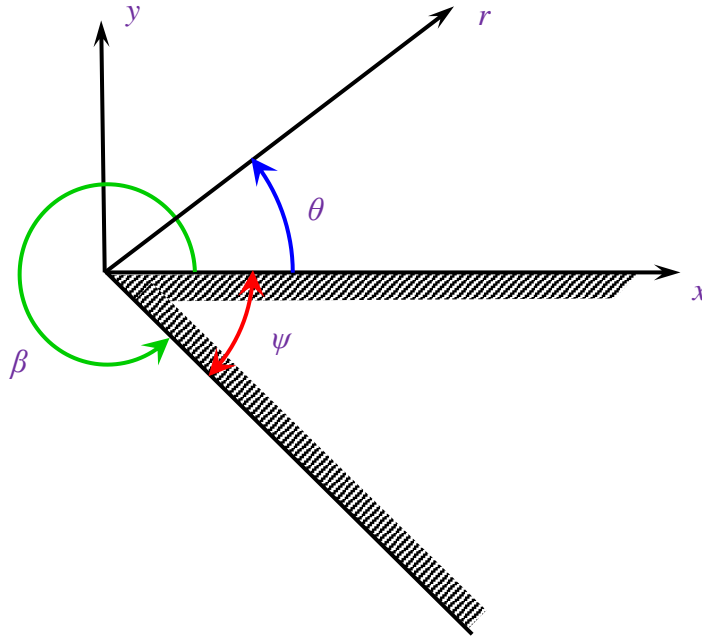

Fig. 3. Definitions and coordinate systems for the corner flow problem.

A domain decomposition strategy is proposed to account for the fact that harmonic

polynomials cannot describe the flow at sharp corners. Using this strategy, the liquid domain is divided into inner and outer subdomains by an artificial boundary. In the inner region, which includes a small area where the sharp corner is present, we use the local corner solution to model the singular property at the apex. In the outer region, the HPC method is applied as usual. Then, the matching conditions are imposed on the artificial boundary.

We introduce artificial boundaries, Σ_m, as matching surfaces, which are represented by dashed lines in Fig. 4. These boundaries divide the fluid domain into a small inner region enclosing the sharp corner and an outer domain with only planar walls. In the original HPC method [22], the liquid domain is first discretized into a finite number of quadrilateral elements, as shown in Fig. 4. However, in this analysis, no mesh is located in the small inner region around the sharp corner, as shown in Fig. 4. In the outer domain, the original HPC method is imposed as usual. On the matching boundaries of Σ_m between the inner and outer domains, the velocity potential and its normal derivatives are matched with the outer domain, which are expressed as follows:

$$\phi_{\text{in}} = \phi_{\text{out}} \quad \text{on} \ \Sigma_m, \tag{13}$$

and

$$\frac{\partial \phi_{\text{in}}}{\partial n} = \frac{\partial \phi_{\text{out}}}{\partial n} \quad \text{on} \ \Sigma_m. \tag{14}$$
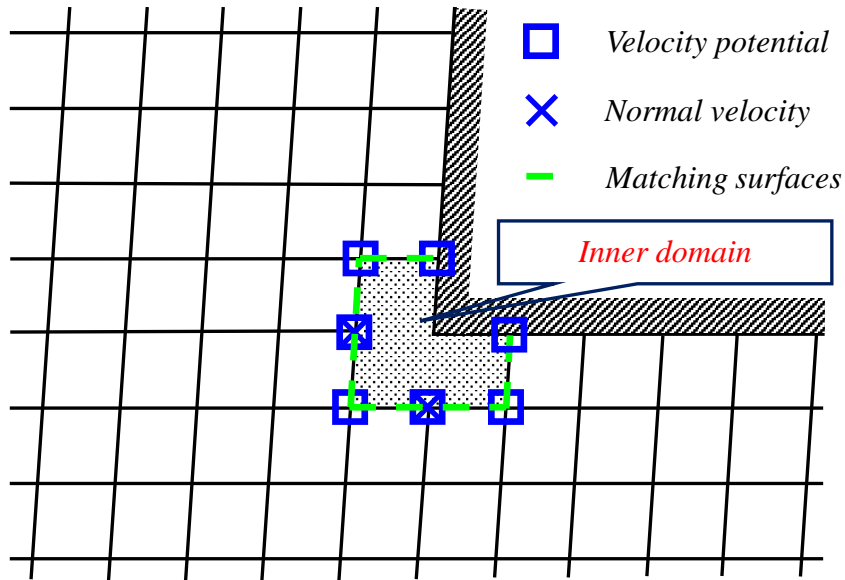

Fig. 4. Schematic of matching boundaries between inner and outer regions.

Eq. (13) and Eq. (14) indicate that the matching condition is met by requiring continuity in the velocity potential on each node and continuity in the normal velocity on matching surfaces,

as illustrated in Fig. 4.

Next, we focus on the sharp corner fully submerged in the fluid, and a 2D transverse section in the Oxy plane is considered. Fig. 4 shows seven nodes on the matching boundaries surrounding the sharp corner. It is assumed that N nodes exist over the fluid domain and only one sharp corner is present. Therefore, $N - 7 + 2$ equations can be established that include the continuity equation in the fluid domain and the conditions at the boundaries (the body boundary condition is imposed at the intersection between the matching boundary and the body surface). Regarding the matching conditions enforced at the matching boundaries, continuity of the velocity potentials at the seven nodes distributed on the matching boundaries is required, as expressed in Eq. (13). Then, the continuity in the normal velocity component, which is described by Eq. (14), is satisfied at two nodes on the matching boundaries, as shown in Fig. 4. Therefore, $N - 7 + 2 + 7 + 2 = N + 4$ equations and $N + 4$ unknowns are needed. In addition to the N unknowns for each node, four unknowns are needed to determine the equation system. Therefore, four unknown coefficients should be included in the corner solution. Thus, in the inner region, where geometrical complications occur, we expand the velocity potential for small r up to the third order, which can be expressed as follows:

$$\phi_{\text{in}} = Ux + Vy + c_0 + \sum_{j=1}^{3} c_j r^{m_j} \cos\left(m_j \theta\right),\tag{15}$$

where U and V denote the instantaneous horizontal and vertical translating velocity components of the body at the sharp corner, respectively. Furthermore, $Or\theta$ is a local polar coordinate system with its origin at the apex. In Eq. (15), the first two terms of the solution are used to address a non-homogenous body boundary condition, and the rest of the solution satisfies the Laplace equation and should satisfy the homogenous body surface condition. Thus, m_j is expressed as follows:

$$m_j = \frac{j\pi}{2\pi - \psi}.\tag{16}$$

Until now the coefficients c_0, c_1, c_2 and c_3 are unknown and should be determined by enforcing the matching conditions at the matching surface, as described in Eq. (13) and Eq. (14). Then, we can establish a linear equation system by coupling the HPC method applied in the outer domain and the local potential flow solution in the inner region.

4   Double-layer nodes technique in HPC

The lifting problem for a foil is important for airplanes and, for example, hydrofoil supported vessels. The shed vorticity from the trailing edge of the foil considered in our studies is assumed concentrated in a free shear layer with a thickness of zero. The fact that the pressure is continuous across the free shear layer provides a condition for expressing the rate of change of

the increasing velocity potential across the free shear layer with time. This condition indicates that the velocity potential is discontinuous across the free shear layer with a thickness of zero. Therefore, two velocity potentials exist on the node on the free shear layer. When using the original HPC method, the velocity potential is assumed continuous everywhere and the velocity potential on a node is single-valued, which prevents the jump condition from being implemented.

Thus, the velocity potential jump is modeled using a double-layer nodes technique that involves the coincidence of two nodes with different velocity potentials. Fig. 5 and Fig. 6 are relevant for this study, in which the free shear layer condition is linearized and imposed on a straight line.
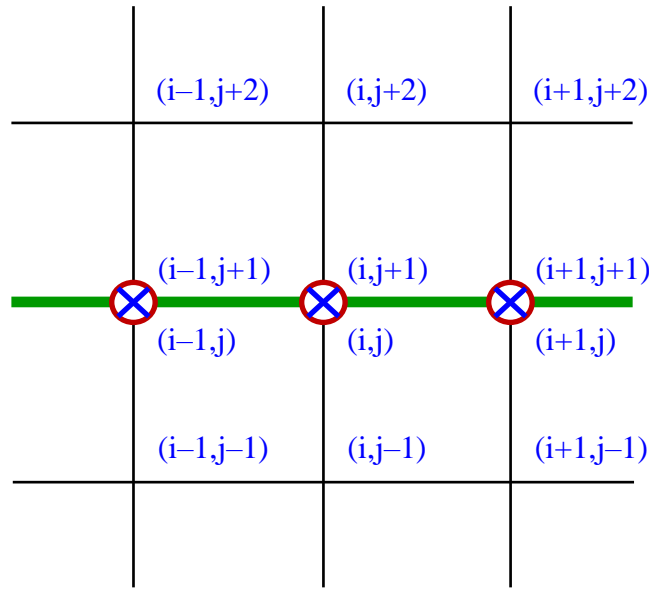

Fig. 5. Schematic of the double-layer nodes.

The zero-pressure jump solution at the free shear layer can alternatively be expressed in terms of Γ_W as follows:

$$\phi_+ - \phi_- = \Gamma_W, \tag{17}$$

where ϕ_+ and ϕ_- denote the velocity potentials on the upper and lower sides of the thin free shear layer, respectively, and Γ_W is the circulation, as defined in Fig. 6.
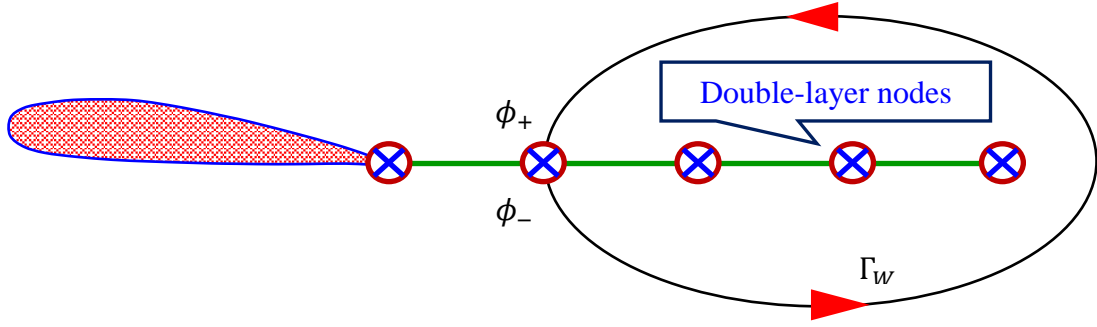
Fig. 6. Schematic of a foil with a wake modeled by double-layer nodes and the definition of the circulation $\Gamma_W = \phi_+ - \phi_-$.

Two conditions are required because there are two nodes on one point of the wake. Apart from the first condition given by Eq. (17), the other condition states that the normal velocity across the free shear layer is continuous, which is expressed as follows:

$$\frac{\partial \phi_+}{\partial n} - \frac{\partial \phi_-}{\partial n} = 0. \tag{18}$$

On the trailing edge, the body boundary condition is satisfied on both sides of the foil. In addition, the Kutta condition requires that the flow leave the trailing edge of the foil smoothly at a finite velocity.

If we consider a foil with zero thickness, the double-layer nodes technique is applied to the foil to represent the pressure difference and velocity potential jump, and the body boundary condition is satisfied on both sides of the foil. Furthermore, the flow at the leading edge is singular for a foil with zero thickness. Therefore, the local potential flow solution described in Section 3 is introduced in a small fluid domain enclosing the leading edge.

5 Results and discussions

In this section, we address several marine hydrodynamics problems by implementing the 2D HPC method coupled with the proposed algorithms. Throughout the study, free-surface-fitted and body-fitted grids are adopted.

5.1 Sharp corner problem

In this subsection, a domain decomposition strategy that combines a local non-analytical potential flow solution and the HPC method (see Section 3) is applied to investigate the hydrodynamic loads exerted on bodies with sharp corners.

5.1.1 A double-wedge oscillating in infinite fluid

As a benchmark verification test, the heave added mass of a double-wedge in infinite fluid, as shown in Fig. 7 (a), is calculated first, and the result is compared with the following analytical solution [10]:

$$A_{33} = \frac{2\rho(0.5B\tan\theta)^2}{\tan\theta}\left[\frac{\pi}{\sin\theta}\frac{\Gamma(1.5-\theta/\pi)}{\Gamma^2(1.0-\theta/\pi)\times\Gamma(0.5+\theta/\pi)}-1\right], \qquad (19)$$

where B and θ are the beam and deadrise angles of the double-wedge, as shown in Fig. 7 (a), and $\Gamma(\cdot)$ denotes the Gamma function [1].

In this problem, four corners exist when the deadrise angle is greater than zero and two sharp corners exist when the deadrise angle is zero. If the deadrise angle is not zero, local potential flow solutions are imposed on all four corners. When the deadrise angle is zero, the double-wedge becomes a flat plate with zero thickness. In this case, the double-layer nodes illustrated in Section 4 are used to model the pressure difference across the upper and lower surfaces of the plate. In addition, local corner solutions should be added on the two ends of the plate.

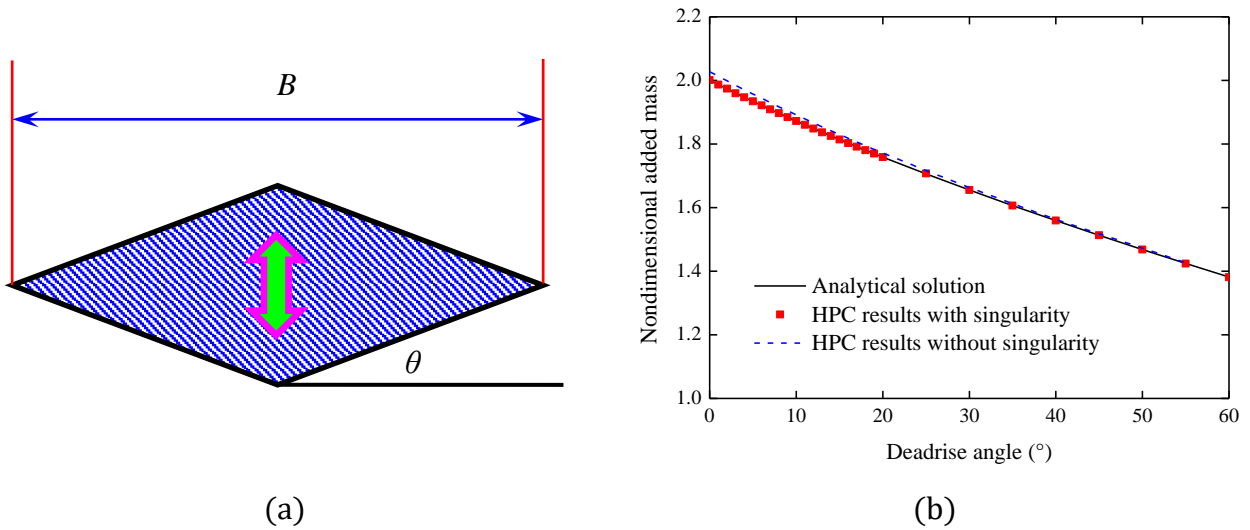| (a) | (b) |

Fig. 7. A double-wedge oscillating in infinite fluid. (a) Main dimensions of the double wedge; (b) Non-dimensional heave added mass varying with the deadrise angle. $A_{33} =$ heave added mass. Non-dimensional heave added mass $= 8A_{33}/(\rho\pi B^2)$. $B =$ beam. $\theta =$ deadrise angle.

Fig. 7 (b) compares the normalized heave added mass $A_{33}/(\rho\pi B^2/8)$ that was calculated using the proposed method with the analytical results given by Eq. (19). In addition, the numerical results, excluding the singular velocity effect at the sharp corner, are considered in Fig. 7 (b). In this case, 160 elements are uniformly distributed over each side of the double-wedge. When the deadrise angle is greater than $30°$ and less than $60°$, a grid system with grid lines paralleling the edge of the double-wedge is used. When the deadrise angle is smaller than $30°$,

a nearly orthogonal grid system is adopted. In addition, the HPC results accounting for the singularities at sharp corners agree with the analytical solution for all deadrise angles and the relative error is $O(10^{-4})$. However, the numerical results without the singular effect are slightly higher than the analytical result if the same type of grid size is applied, and the corresponding difference reaches up to 1.0%. Therefore, the present HPC method coupled with the local corner solution can yield results that are more accurate.

5.1.2   A floating heaving rectangular cylinder

In this section, a linear frequency-domain analysis, which was introduced in Section 2.3, is conducted by considering a heaving rectangular cylinder on a free surface. The beam and draft of the rectangular cylinder are denoted as B and D, respectively. The local solution has been added at the sharp corners. In this problem, the water depth is assumed infinite. However, because the present approach involves using a field solver, the water depth h is finite. To minimize the effects of the bottom, we set the water depth h as the maximum value between twenty times the draft of the rectangle and twice the wavelength of the radiated waves. The wavelength is related to the heaving frequency, which means that lower frequencies correspond with larger wavelengths. When the heaving frequency is very low, the horizontal length of the computational domain is exceedingly large.

To reduce the computational effort required, the symmetry property of the rectangular cylinder is used; thus, only half of a section is considered, as shown in Fig. 8. No horizontal velocity component exists on the symmetry plane; therefore, $\partial\phi/\partial x = 0$. In addition, we can use the domain decomposition strategy to reduce the number of unknowns in the horizontal direction. Inspired by Yeung [30], we can introduce an artificial matching boundary, Σ_+, as shown in Fig. 8. In this problem, we set the matching boundary Σ_+ at twice the wavelength from the rectangular cylinder. In the inner region on the left side of the matching boundary, the velocity potential is described using the HPC method. In the outer domain on the right side of the matching boundary, the velocity potential ϕ_+ can be written in terms of eigen-function expansions that satisfy the governing equation, the linearized free-surface boundary condition in the frequency domain and the bottom condition.

If the present problem is time-harmonic and at the steady state, we can separate the space and time variables in the velocity potential ϕ_+ as follows:

$$\phi_+\left(x,y,t\right)=\Re\left\{\varphi\left(x,y\right)\cdot e^{i\omega t}\right\} \quad \text{with} \quad \varphi\left(x,y\right)=\varphi_R+i\varphi_I. \tag{20}$$
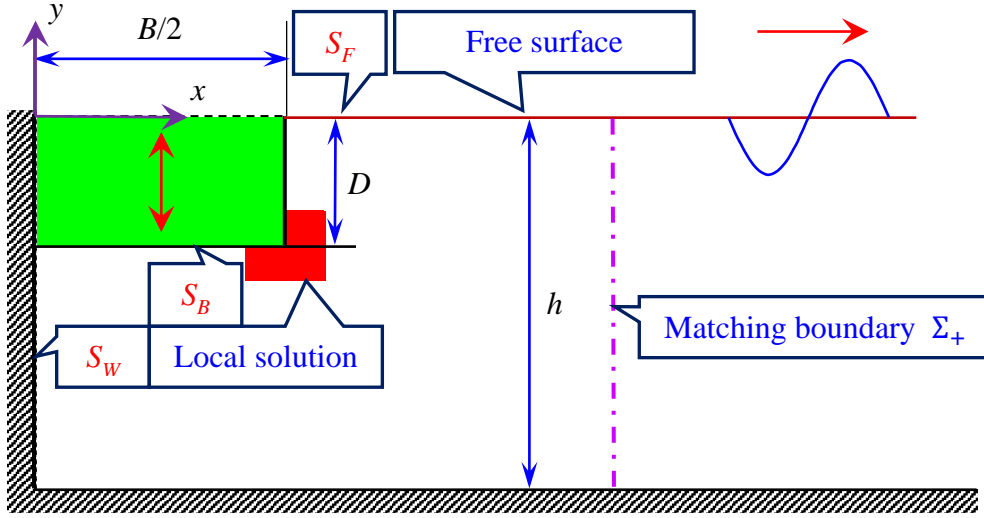
Fig. 8. Schematic of a half rectangular section heaving on a free surface.

Then, the governing equation and boundary conditions with respect to $\varphi(x,y)$ in the frequency domain are expressed as follows:

$$\frac{\partial^2\varphi}{\partial x^2}+\frac{\partial^2\varphi}{\partial y^2}=0,$$

$$-\omega^2\varphi+g\frac{\partial\varphi}{\partial y}=0 \qquad \text{at } y=0, \qquad (21)$$

$$\frac{\partial\varphi}{\partial y}=0 \qquad \text{at } y=-h.$$

Moreover, we should incorporate the radiation condition in which the radiated waves propagate outwards as follows:

$$\frac{\partial\varphi}{\partial x}+\mathrm{i}k\varphi\to 0 \qquad \text{when } x\to+\infty, \qquad (22)$$

where k denotes the wave number, and

$$\omega^2=kg\tanh kh, \qquad (23)$$

is the dispersion relation. The eigen-function expansions can be expressed as follows [30]:

$$\varphi=\left(C_0^R+\mathrm{i}C_0^I\right)\exp\left(-\mathrm{i}k_0 x\right)\frac{\cosh k_0\left(y+h\right)}{\cosh k_0 h}+\sum_{j=1}^{N_E}\left(C_j^R+\mathrm{i}C_j^I\right)\exp\left(-k_j x\right)\cos k_j\left(y+h\right), \qquad (24)$$

where the eigenvalues k_0 and $\mathrm{i}k_j$ are roots of the dispersion function described by Eq. (23). In Eq. (23), k represents either k_0 or $\mathrm{i}k_j$, and N_E denotes the number of the expansion terms. The coefficients C_j^R and C_j^I $(j=0,1,\dots)$ are determined from the matching conditions

14

imposed on the matching boundary Σ_+, as shown in Fig. 9.

The matching condition enforced on Σ_+ involves the continuity of the velocity potential and the normal velocity component on the matching boundary. In this problem, the continuity in the velocity potential is imposed on all grid points at the matching boundary Σ_+, as demonstrated in Fig. 9. However, the continuity in the normal velocity component cannot be satisfied over the entire boundary to ensure that the equation system is determined. Hence, we select the grid points nearest the free surface to enforce the matching condition associated with the normal velocity component, as illustrated in Fig. 9. In addition, the number of expansion terms with respect to the evanescent modes N_E should be less than the number of nodes at the vertical matching boundary N_y. Therefore, a linear equation system can be established with fewer unknowns.
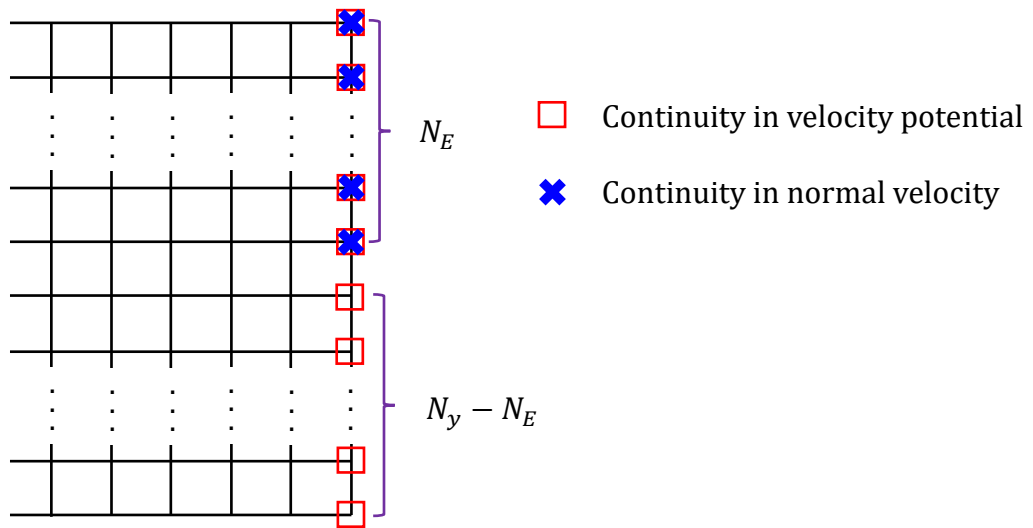

Fig. 9. Schematic of matching conditions. N_E = number of expansion terms with respect to evanescent modes. N_y = number of nodes on the vertical matching surface.

Because the corner solution given by Eq. (15) is only valid in a small region, grid points are non-uniformly distributed over the side of the rectangle and the cosine distribution is applied with fine grids distributed near the corner, as shown in Fig. 10. To avoid abrupt changes in the grid size, the cosine distribution in both horizontal and vertical directions is implemented when the distance from the rectangle is less than the length of the semi-breadth and draft.
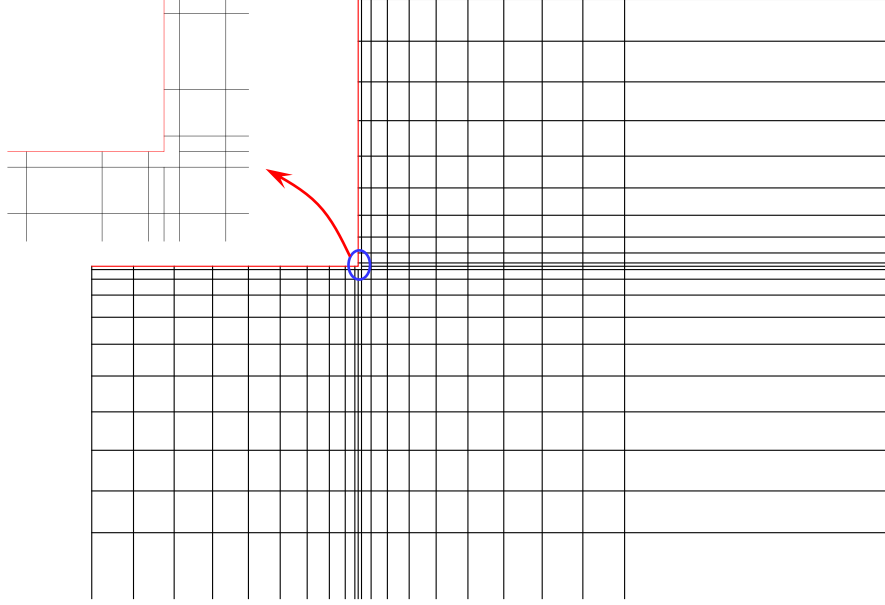
Fig. 10 Schematic of the non-uniform distribution over the body.

In Fig. 11, the convergence of eigen-function expansions is tested using a beam-to-draft ratio B/D of 2.0 and a non-dimensional square of the oscillation frequency of $\omega^2 B/(2g) = 1.0$. The horizontal distance between the rectangular cylinder and the matching boundary is twice the wavelength of the radiated waves. The number of the expansion terms ranges from $N_E = 0$ to 60, which indicates that the number of expansion terms does not affect the added mass and damping associated with the linear wave force or the second-order mean vertical force. This result occurs because the distance from the rectangle to the vertical matching boundary is far enough to attenuate the evanescent modes.
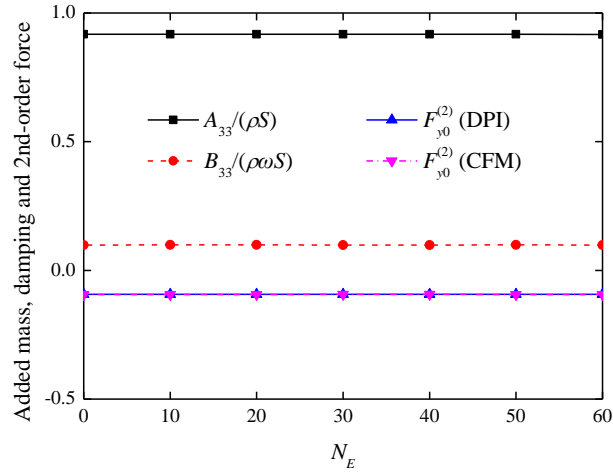

Fig. 11. The convergence behaviors of eigen-function expansions with a forcing frequency given by $\omega^2 B/(2g) = 1.0$. A_{33} = heave added mass. B_{33} = heave damping. S = submerged cross-sectional area. ρ = mass density of liquid. ω = circular frequency. The normalized second-order mean vertical force $F_{y0}^{(2)} = F_y^{(2)}/(\rho\omega^2\eta_{3a}^2 B)$. $F_y^{(2)}$ = second-order mean vertical force.

16

$B =$ beam. $\eta_{3a} =$ heave amplitude. $N_E =$ number of eigen-expansions. DPI = direct pressure integration. CFM = conservation of fluid momentum.
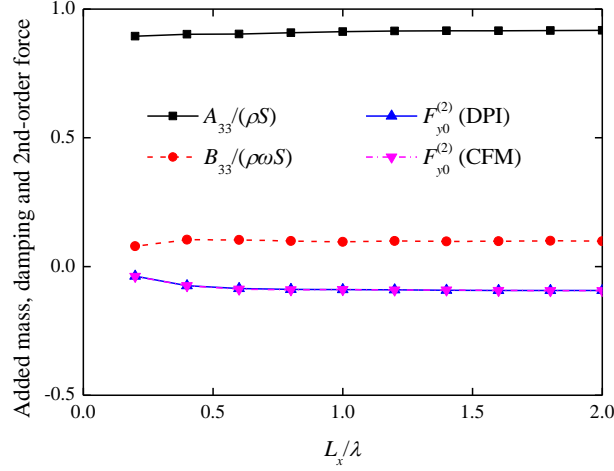

Fig. 12. Convergence performance of the horizontal length of the computational domain with a forcing frequency given by $\omega^2 B/(2g) = 1.0$. $A_{33} =$ heave added mass. $B_{33} =$ heave damping. $S =$ submerged cross-sectional area. $\rho =$ mass density of liquid. $\omega =$ circular frequency. The normalized second-order mean vertical force $F_{y0}^{(2)} = F_y^{(2)}/(\rho\omega^2\eta_{3a}^2 B)$. $F_y^{(2)} =$ second-order mean vertical force. $B =$ beam. $\eta_{3a} =$ heave amplitude. $L_x =$ horizontal length from the rectangle to the matching boundary. $\lambda =$ wavelength of radiated waves. DPI = direct pressure integration. CFM = conservation of fluid momentum.

Fig. 12 demonstrates the convergence behaviors of the horizontal distance from the rectangle to the matching boundary. The beam-to-draft ratio (B/D) of the rectangle is equal to 2.0, and the non-dimensional square of the oscillation frequency is given by $\omega^2 B/(2g) = 1.0$. The abscissa is the ratio of the horizontal distance L_x to the wavelength λ of the radiated waves, and the ordinate includes the added mass, damping and second-order mean vertical force. In this example, the number of expansion terms with respect to the evanescent mode N_E is equal to 50. Convergence can be achieved when the ratio of the horizontal distance L_x to the wavelength λ is greater than 1.6.

Therefore, in the following numerical examples, the number of expansion terms with respect to the evanescent modes in Eq. (23) is $N_E = 50$, and the horizontal distance between the rectangle and the vertical matching boundary is twice the wavelength of the radiated waves.
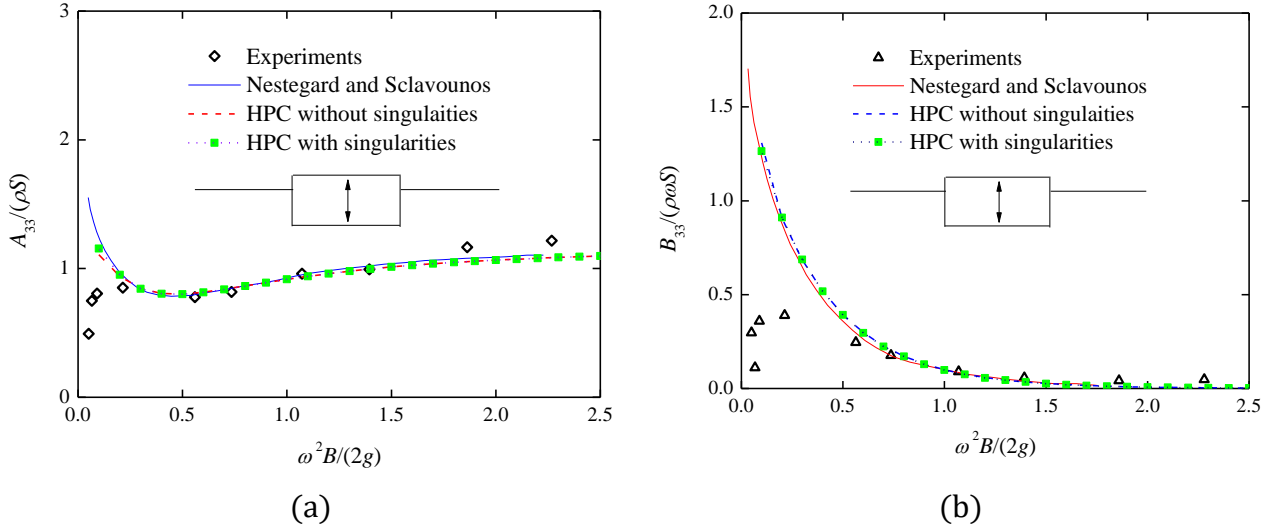
Fig. 13. Heave added mass and damping versus the frequency of a floating rectangular section with a beam-to-draft ratio (B/D) of 2.0. (a) Added mass; (b) Damping. B = beam. D = draft. A_{33} = heave added mass. B_{33} = heave damping. S = submerged cross-sectional area. ρ = mass density of liquid. ω = circular frequency.

Fig. 13 presents the heave added mass and damping versus frequency of a rectangular section with a beam-to-draft ratio B/D of 2.0. In addition to the results accounting for the singularity at the sharp corner, the numerical results without the singular flow effect are also presented. These results were compared with the experimental results presented by Vugts [25] and the numerical potential flow calculations conducted by Nestegard and Sclavounos [20]. The calculation method reported in [20] is based on Ursell [24] and is performed by coupling the BEM and multipole expansions. However, the singularity at the sharp corner is not considered. Fig. 13 shows small differences in the results with and without the singular flow effect. In addition, the agreement of these results with the calculations conducted by Nestegard and Sclavounos [20] is rather satisfactory. The comparison with the experimental results reported by Vugts [25] is not satisfactory at low frequencies. When the forcing frequency is low $\omega^2 B/(2g) < 0.25$, experimental inaccuracies will occur because a small absolute error in the measured force can result in large deviations in the added mass and damping coefficients in this range [25]. Furthermore, because flow separation from the sharp corner will occur, it is impossible to attain perfect agreement with the experiments.

5.1.3 Second-order mean vertical force of a heaving floating rectangle

Based on the foregoing analysis, the potential flow added mass and damping for a body with sharp corners involving the singular flow effect are not very different from those obtained for a body for which this effect is excluded. One reason for this similarity is that the velocity potential is finite at the sharp corner. In addition, the added mass and damping are determined by integrating the velocity potential times the relevant normal component over the mean wetted

body surface. However, if we focus on the hydrodynamic loads associated with the velocity components, such as the second-order hydrodynamic force due to the quadratic velocity term in Bernoulli's equation, the singular flow effect at the sharp corner is expected to play a more important role.

Therefore, we investigate the second-order mean vertical force experienced by a heaving rectangular cylinder, as shown in Fig. 8. The relevant problem in 3D has been studied by Mavrakos [17]. The second-order force can be calculated using direct pressure integration (DPI) or the conservation of fluid momentum (CFM) [9]. Zhao and Faltinsen [32], who did not account for the flow singularities, showed that the near-field approach based on DPI presents challenges when obtaining converged results if a sharp corner is present, whereas CFM is more robust and efficient.

In principle, the second-order mean vertical force calculated by DPI should be consistent with that based on CFM. The pressure integration around the sharp corner associated with the quadratic terms of the velocities is difficult to evaluate due to the singular properties of the velocity components at the apex. However, the velocity potential and the corresponding velocity components are expressed in the form of a series in this analysis. Furthermore, the series is weakly singular and integrable. Therefore, we can still obtain accurate values by DPI.

Before investigating the second-order mean vertical force, we first study the convergence properties of the original HPC method and the HPC method using singular corner solutions, as demonstrated in Fig. 14. In this numerical example, the non-dimensional square of the oscillation frequency is $\omega^2 B/(2g) = 1.0$, and the ratio between the draft and half-beam $D/(B/2)$ is 1.0. Due to the symmetry properties of the rectangle, only a half section is considered. The abscissa is the number of elements (*NE*) distributed over the half bottom of the rectangle, and the ordinate includes the added mass and damping, which are shown in Fig. 13, and the normalized second-order mean force in the vertical direction, which is defined as $F_{y0}^{(2)} = F_y^{(2)}/(\rho\omega^2\eta_{3a}^2 B)$. On the vertical side of the rectangle, the grid size is the same as that distributed over the half bottom. The results of the added mass, damping and second-order force converge when more than 80 elements are used. In addition, the converged second-order mean vertical force calculated by DPI is consistent with that based on CFM if the singularity at the apex is considered. Nevertheless, differences are always observed if the singularity is excluded, even when more elements are used.
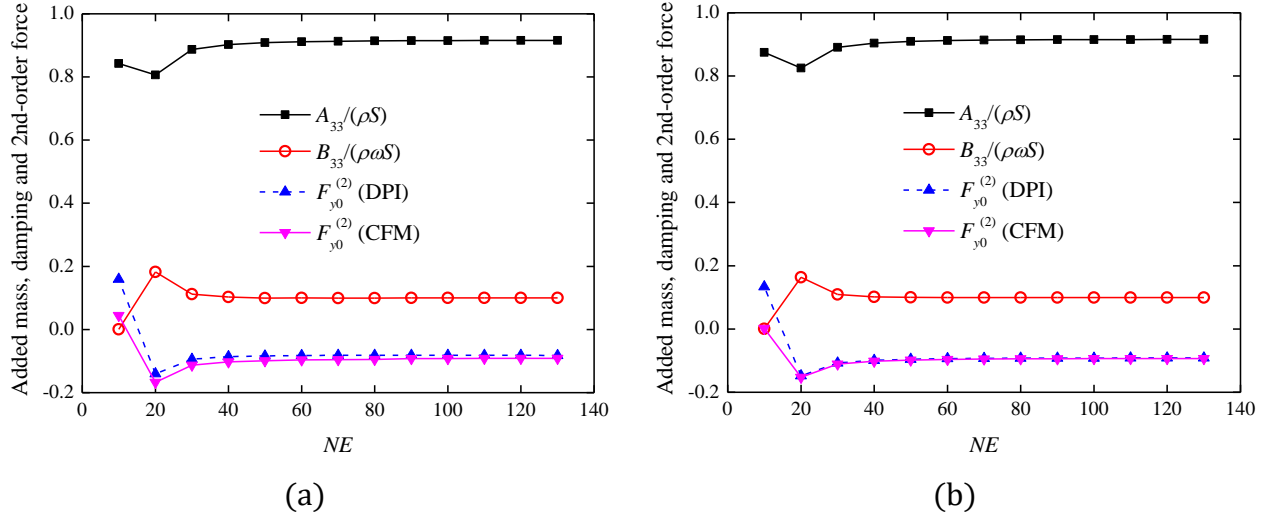
Fig. 14. Convergence characteristics of the algorithm with and without the singular effect for a heaving floating rectangular section with forcing frequency given by $\omega^2 B/(2g) = 1.0$. (a) Original HPC method; (b) HPC method coupled with singular solutions. $A_{33} =$ heave added mass. $B_{33} =$ heave damping. $S =$ submerged cross-sectional area. $\rho =$ mass density of liquid. $\omega =$ circular frequency. The normalized second-order mean vertical force $F_{y0}^{(2)} = F_y^{(2)}/(\rho\omega^2\eta_{3a}^2 B)$. $F_y^{(2)} =$ second-order mean vertical force. $B =$ beam. $\eta_{3a} =$ heave amplitude. $NE =$ number of elements on half bottom of the rectangle. DPI = direct pressure integration. CFM = conservation of fluid momentum.

Fig. 15 shows the frequency dependence of the normalized second-order mean vertical force. In Fig. 15 (a), the singularity at the sharp corner is accounted for by adding the local corner solution but is excluded in Fig. 15 (b). In both subfigures, the grid size is the same, and 100 elements are distributed over one side of the rectangular cylinder. In addition, 600 grid points are distributed over the free surface, S_F, and 500 points are distributed over the vertical symmetry plane, S_W. If we consider the singularity at the sharp corner, as shown in Fig. 15 (a), the results obtained from DPI are consistent with those obtained from CFM. When the singular flow effect is not considered, Fig. 15 (b) shows that the DPI results clearly differ from the CFM results. Therefore, the inclusion of the local singular corner flow enables us to accurately calculate the second-order force associated with the quadratic terms of the velocity components using DPI within potential flow theory. However, the CFM results obtained by neglecting singularities are similar to the CFM results obtained by including the singularities. The latter method is encouraging for the state-of-the-art BEM, which does not account for flow singularities [7, 16].
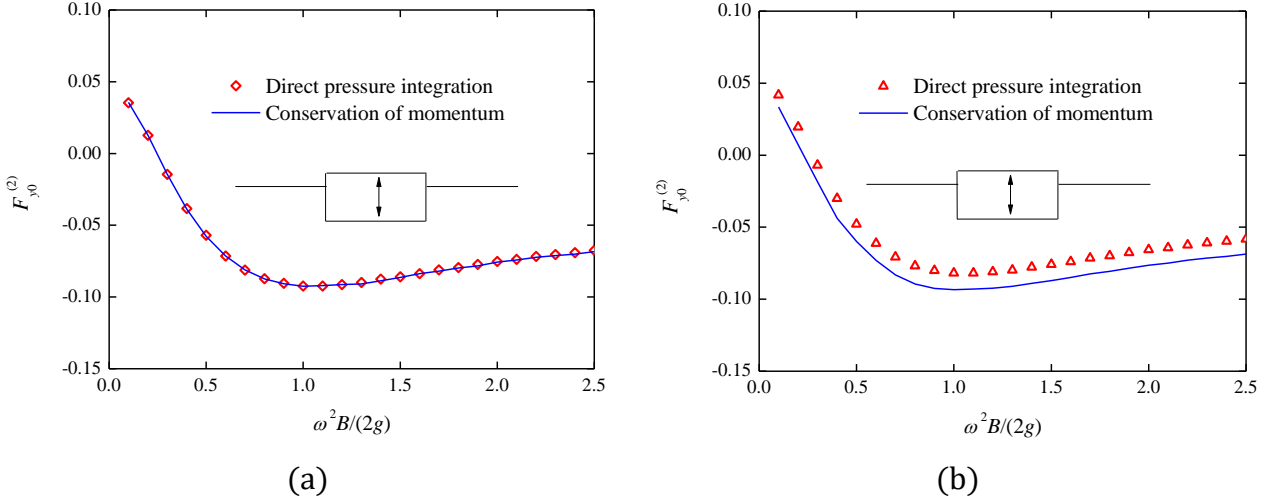
Fig. 15. Normalized second-order mean vertical force of a heaving floating rectangle. (a) Singularity is accounted for; (b) Singularity is excluded. The normalized second-order mean vertical force $F_{y0}^{(2)} = F_y^{(2)}/(\rho\omega^2\eta_{3a}^2 B)$. $F_y^{(2)} =$ second-order mean vertical force. $\rho =$ mass density of liquid. $\omega =$ circular frequency. $B =$ beam. $\eta_{3a} =$ heave amplitude.

5.2 Lifting problem

This subsection presents the numerical results of the lifting problem for a foil based on the double-layer nodes algorithm proposed in Section 4. In numerical examples of a foil in steady and unsteady motions in infinite fluid, the vertical size of the computational domain is 16 times the chord length with the foil located in the middle. The horizontal distance from the upstream boundary to the leading edge of the foil is 8 times the foil's chord length. The distance between the end of the wake to the downstream side is greater than 5 times the chord length.

5.2.1 Steady lifting problem for a flat plate in infinite fluid

To illustrate the merits of the local corner solution presented in Section 3 and validate the double-layer nodes algorithm described in Section 4, we begin by studying the lifting problem for a flat plate in steady flow and infinite fluid. The chord length of the flat plate is denoted as c, and the angle of attack, denoted as α, is 2.0°. The body boundary condition is linearized (see [19]). In this case, the analytical solution of the vortex strength distribution, which is defined as $\gamma(x) = \partial\phi_+/\partial x - \partial\phi_-/\partial x$, exists [19]; thus, we can use this analytical solution to verify the present numerical algorithm. In this problem, 2321×442 grid points are used to discretize the computational domain, and 101 nodes are distributed over each side of the flat plate with cosine distributions near the edges.

First, we employ the usual HPC method that neglects the singularity at the leading edge to study this problem. The corresponding results are demonstrated by the dashed and dotted line shown in Fig. 16. In Fig. 16, the vortex strength is normalized by the ambient flow velocity U.

The numerical results neglecting the singularity at the leading edge clearly deviate from the analytical solution. At the leading edge, the analytical solution goes to infinity. However, the calculated result without the local potential flow solution is finite because the singularity at the leading edge is not well simulated. Next, we consider the singularity at the leading edge, adopt the same type of grid size, and use the local potential flow solution to represent the velocity potential near the leading edge. In the small region enclosing the leading edge, the velocity potential can be expressed analytically; thus, we can determine the vortex strength at any point in this small region. The corresponding results are represented by the dashed line in Fig. 16, and no discrepancy relative to the analytical solution is observed. Therefore, we can estimate the errors of the vortex strength, excluding the cell enclosing the leading edge. When the singularity at the leading edge is accounted for, the mean squared error of the vortex strength distributed over the nodes on the foil relative to the analytical solution is $O(10^{-3})$. However, when the singularity is excluded, the mean squared error is as large as $O(10^{-2})$. Therefore, the double-layer nodes technique can be used to model the discontinuity in the velocity potential that is associated with circulation around the foil, and the local corner solution can adequately represent the singularity.
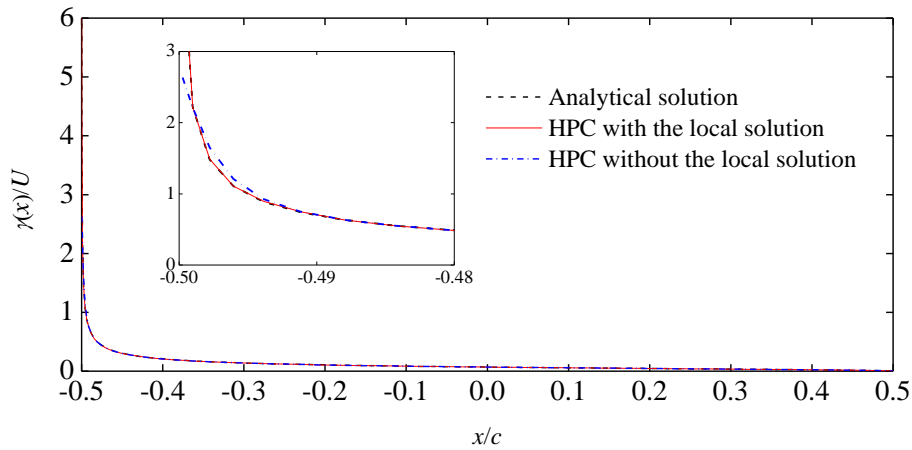

Fig. 16. Normalized vortex strength $\gamma(x)/U$ distribution over a flat plate. $\gamma(x) =$ vortex strength distribution. $U =$ ambient flow velocity. $c =$ chord length of the foil. $x/c = -0.5$ is the leading edge and $x/c = 0.5$ is the trailing edge. The angle of attack α is 2°. The present results accounting for the singularity at the leading edge are compared with those obtained by excluding the singularity and the analytical solution.

5.2.2 Unsteady lifting problem for a flat plate in infinite fluid: Transient problem

In this section, the linear transient problem for a flat plate in infinite fluid with a thickness of zero and a nonzero angle of attack starting instantaneously from rest and to a constant velocity is studied (see [19]). The resulting lift force divided by the steady force is the Wagner function, which depends on the non-dimensional time $s = Ut/c$, where U is the ambient flow velocity

and t represents time. The Wagner function is analytically expressed as follows [6]:

$$W(s) = \frac{2}{\pi} \int_0^\infty \frac{F(k)}{k} \sin(ks) \, dk, \tag{25}$$

with

$$F(k) = \Re \left[\frac{H_1^{(2)}(k)}{H_1^{(2)}(k) + iH_0^{(2)}(k)} \right], \tag{26}$$

where the Hankel function $H_n^{(2)}(k)$ is a combination of the first and second types of Bessel functions, i.e., [1]

$$H_n^{(2)}(k) = J_n(k) - iY_n(k). \tag{27}$$

The method used to efficiently and accurately compute the improper integral with the oscillatory integrand given by Eq. (25) can be found in Appendix A. For numerical implementation, the double-layer nodes technique is applied to the linearized position of the free shear layer with a thickness of zero and the linearized position of the foil with a thickness of zero, except at the leading edge. In the region enclosing the leading edge, the local potential flow solution is imposed. Because the pressure jump across the free shear layer is zero, the following relationship is obtained:

$$\begin{aligned}
0 &= p_+ - p_- \\
&= -\rho \left[\frac{\partial(\phi_+ - \phi_-)}{\partial t} + U \frac{\partial(\phi_+ - \phi_-)}{\partial x} \right] \\
&= -\rho \left(\frac{\partial \Gamma_W}{\partial t} + U \frac{\partial \Gamma_W}{\partial x} \right),
\end{aligned} \tag{28}$$

where, according to the linearized Bernoulli's equation, p_+ and p_- denote the pressure on the upper and lower double-layer nodes on the thin free shear layer, respectively. In addition, $\Gamma_W = \phi_+ - \phi_-$ is the circulation around a curve enclosing the wake downstream of the investigated double-layer nodes, as illustrated in Fig. 6. The general solution of Eq. (28) is expressed as follows:

$$\Gamma_W(x,t) = \Gamma_W(x - Ut), \tag{29}$$

which indicates that the circulation Γ_W is advected downstream with an ambient flow velocity of U and remains constant. Therefore, the horizontal length of the grid downstream should be uniform, and the grid length should be $U\Delta t$, where Δt represents the time step and the circulation $\Gamma_W = \phi_+ - \phi_-$ is advected by the length of the grid downstream. To be consistent with the transient theory of the lifting problem in infinite fluid [6], the strength of the starting

23

vortex is zero. At the trailing edge, the body boundary condition is satisfied on both sides of the foil. In addition, the Kutta condition given by Eq. (17) is imposed. Using this method, we can calculate the time history of the lift coefficient and the resulting lift coefficient normalized by the steady-state results $C_L/C_L(t = \infty)$. Fig. 17 compares the present numerical results and the analytical solution given by Eq. (25), which agree with a relative difference is $O(10^{-3})$. During the numerical implementation, a grid size of 1451×442 with cosine distributions near the edges is used to model this problem. As described for the steady problem in Section 5.2.1, the foil is divided into 100 portions.
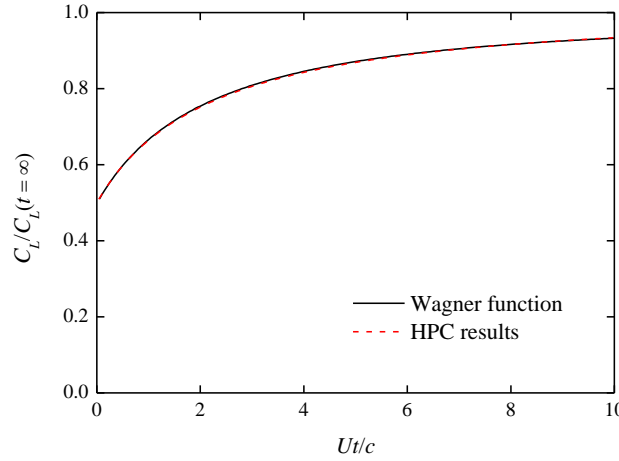

Fig. 17. Ratio $C_L/C_L(t = \infty)$ between instantaneous lift and steady lift for a 2D flat plate with small angle of attack versus non-dimensional time Ut/c based on linear theory. $C_L =$ instantaneous lift coefficient. $C_L(t = \infty) =$ steady lift coefficient. $U =$ ambient flow velocity. $c =$ chord length. A comparison with the calculated analytical solution expressed by the Wagner function is made.

5.2.3   Harmonic oscillations of a flat plate in infinite fluid

As a continuation of the analysis of the transient lifting problem in infinite fluid, unsteady linearized lifting problems for a flat plate with harmonic heave and pitch motions are considered herein (see [19]). Here, pitch motions with a circular frequency of ω are denoted as follows:

$$h(t) = \Re\left(h_0\, e^{i\omega t}\right) \quad \text{and} \quad \alpha(t) = \Re\left(\alpha_0\, e^{i\omega t}\right), \tag{30}$$

where $h(t)$ and $\alpha(t)$ are the instantaneous displacement and attack angle of the foil and h_0 and α_0 represent the amplitudes of the heave and pitch motions, respectively. For this oscillatory time dependence problem with an assumed chord length of 2.0, the analytical expression of the lift force at steady-state is expressed as follows [19]:

$$L = -2\pi\rho U^2 \Re\left\{e^{i\omega t} C(k_r)\left[ik_r h_0 - \left(1 + \frac{1}{2}ik_r\right)\alpha_0\right]\right\} - \pi\rho\left(\ddot{h} - U\dot{\alpha}\right), \tag{31}$$

where $k_r = \omega c/(2U)$ represents the reduced frequency and $C(k_r)$ denotes the Theodorsen function [6], which is expressed as

$$C(k_r) = \frac{H_1^{(2)}(k_r)}{H_1^{(2)}(k_r) + iH_0^{(2)}(k_r)}. \tag{32}$$

In Fig. 18, the time history of the lift coefficient C_L is presented for different reduced frequencies, and the present numerical results and the analytical solution are compared. In addition, the non-dimensional heave and pitch motion amplitudes are $h_0/c = 0.05$ and $\alpha_0 = -1.0°$, respectively. The grid resolution is the same as the numerical example present in Section 5.2.2. In the present numerical study, the transient portion is involved because the foil begins at rest and suddenly reaches a constant velocity. However, the analytical solution assumes steady-state conditions. When nearly steady-state conditions are reached, the agreement with the analytical solution is good.
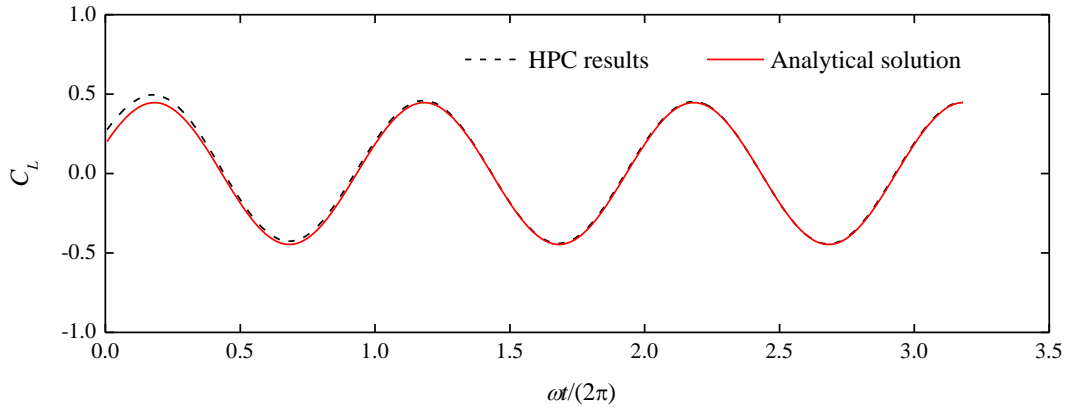
(a)
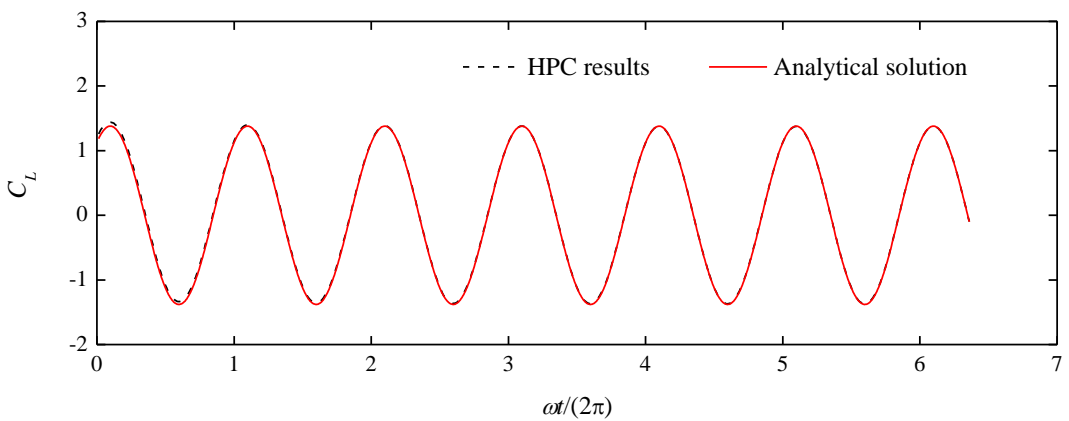
(b)

Fig. 18. The instantaneous lift coefficient of a foil during heave and pitch motions versus non-dimensional time calculated in the time domain using the HPC method and the steady-state analytical results of Theodorsen. (a) $k_r = 2$; (b) $k_r = 4$. $C_L = L/0.5\rho U^2 c$. $C_L =$ lift coefficient. $L =$ lift force. $\rho =$ mass density of liquid. $U =$ ambient flow velocity. $c =$ chord length. $k_r =$

$\omega c/(2U)$. $k_r =$ reduced frequency. $\omega =$ circular frequency.

5.2.4 Hydrodynamic behavior of a steadily translating hydrofoil

The flow about a NACA-4412 hydrofoil that steadily operates beneath a free surface is considered, as shown in Fig. 19. The submergence depth, water depth and angle of attack are denoted as h, d and α, respectively. Here, the submergence depth is the distance between the trailing edge of the hydrofoil and the mean free surface. An inertial Cartesian coordinate system, Oxy, translated with the hydrofoil at a speed of $-U$ with respect to the Earth-fixed coordinate system is established using the $Ox-$axis that coincides with the undisturbed free surface. The $Oy-$axis is positively oriented upwards. The free-surface boundary condition is linearized, but the body boundary condition is satisfied exactly. For a NACA hydrofoil with nonzero thickness at the trailing edge, we extend the upper and lower surfaces at the trailing edge until intersection and obtain a hydrofoil with a trailing edge thickness of zero (see Fig. 20). The wake, which is attached to the new trailing edge with zero thickness, is linearized and imposed on a straight line. We use the modified hydrofoil to investigate the lifting problem. When calculating the hydrodynamic force on the hydrofoil, we only integrate the pressure over the original hydrofoil surface.
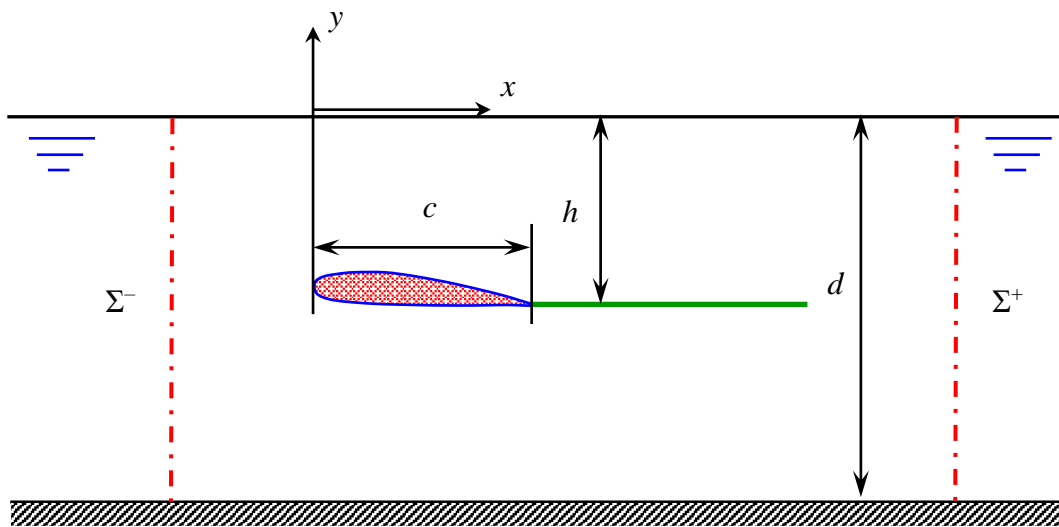

Fig. 19. Schematic of a hydrofoil operating under a free surface and the main dimensions.
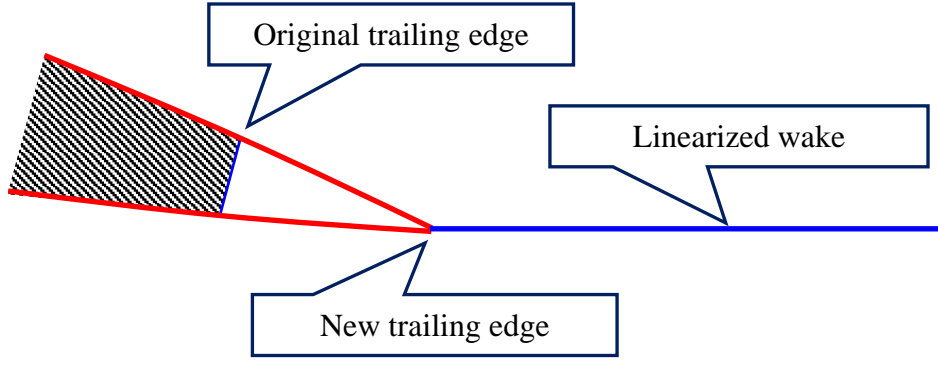
Fig. 20. Schematic of a NACA hydrofoil with nonzero thickness at the trailing edge and a modified hydrofoil with a trailing edge thickness of zero.

To reduce the number of grid points, a domain decomposition strategy is adopted. Following the study by Yeung and Bouger [31], we introduce two vertical artificial boundaries, Σ_- and Σ_+, as shown in Fig. 19. The two boundaries separate the inner domain in which all geometrical complications occur from two outer domains on the upstream and downstream sides, respectively. Waves only occur in the downstream domain. The velocity potential can be expressed as eigen-function expansions that satisfy the governing equation, linearized free-surface condition and bottom condition, which are expressed as follows:

$$
\begin{aligned}
&\frac{\partial^2 \phi_\pm}{\partial x^2} + \frac{\partial^2 \phi_\pm}{\partial y^2} = 0, \\
&U^2 \frac{\partial^2 \phi_\pm}{\partial x^2} + g \frac{\partial \phi_\pm}{\partial y} = 0 \qquad \text{at} \quad y = 0, \\
&\frac{\partial \phi_\pm}{\partial y} = 0 \qquad \text{at} \quad y = -h,
\end{aligned}
\tag{33}
$$

where ϕ_+ and ϕ_- denote the velocity potentials in the outer regions on the downstream and upstream sides, respectively. Then, the eigen-function expansions satisfying the radiation condition are expressed as follows [31]:

$$
\begin{aligned}
\phi^\pm = C_0^\pm &+ H(x) H\left(1 - Fr_h\right)\left(C_c \cos k_0 x + C_s \sin k_0 x\right) \frac{\cosh k_0(y+h)}{\cosh k_0 h} \\
&+ \sum_{j=1}^{N_E} C_j^\pm \exp\left(\mp k_j x\right) \cos k_j(y+h),
\end{aligned}
\tag{34}
$$

where Fr_h is the depth Froude number $Fr_h = U/\sqrt{gh}$, and $H(x)$ denotes the Heaviside function, which is equal to 1 when $x \geq 0$ and 0 when $x < 0$. Furthermore, Eq. (34) on the downstream side is only valid downstream of the vortex sheet. The eigen-values k_0 and ik_j are roots of the dispersion function

$$k = \nu \tanh kh, \tag{35}$$

where k represents either k_0 or ik_j; N denotes the number of expansion terms; and $\nu = g/U^2$. Here, we set $N_E = 50$, and a grid size of 1260×242 is used. The coefficients C_c, C_s and $C_j^{\pm}$ ($j = 0, 1, \dots$) are determined from the matching conditions that require continuity of the velocity potential and normal velocity imposed on the matching boundaries Σ_- and Σ_+. The continuity in the velocity potential is imposed on all grid points on the matching boundaries, and the continuity in the normal velocity component is only enforced on the selected grid points near the free surface. In contrast with the harmonic oscillation problem described in Section 5.1.2, the free-surface boundary condition for the present steady translation problem involves a second-order derivative with respect to the velocity potential ϕ, as depicted in Eq. (33). In addition, the free-surface boundary condition is not enforced at the intersection point between the free surface and the matching boundary according to [31]. Therefore, the continuity of the second-order derivative $\partial^2 \phi / \partial x^2$ should be imposed on the intersection node between the matching boundary and the free surface [31].

Furthermore, due to the abrupt disappearance of the wake, a free-surface disturbance is present, which can be represented by a steadily translating point vortex attached to the end of the wake under a free surface with the location of the end of the wake defined by (x_V, y_V). Then, the velocity potential at a field point (x, y) induced by a point vortex located at (x_V, y_V) with strength Γ is [26]:

$$
\begin{aligned}
\phi_V = {} & \frac{\Gamma}{2\pi} \arctan\left(\frac{y - y_V}{x - x_V} \right) - \frac{\Gamma}{2\pi} \arctan\left(\frac{y + y_V - 2h}{x - x_V} \right) \\
& - \frac{\Gamma}{\pi} \mathrm{PV} \int_0^\infty \frac{k + \nu}{k} e^{-kh} \frac{\sinh k(y_V + h)\cosh k(y + h)}{\nu \sinh kh - k \cosh kh} \sin k(x - x_V)\, \mathrm{d}k \\
& + \frac{\Gamma \nu}{k_0} \frac{\sinh k_0(y_V + h)\cosh k_0(y + h)}{\nu h - \cosh^2 k_0 h} \cos k(x - x_V) + \frac{\Gamma \nu(y_V + h)}{2(\nu h - 1)}.
\end{aligned}
\tag{36}
$$

When imposing the matching conditions on the boundary Σ_+, the effects from the point vortex should also be accounted for. Here, the strength of the point vortex Γ is equal to $-\Gamma_W$, and no additional variables are introduced. The algorithm for evaluating the principle value integral in Eq. (36) is presented in Appendix B.
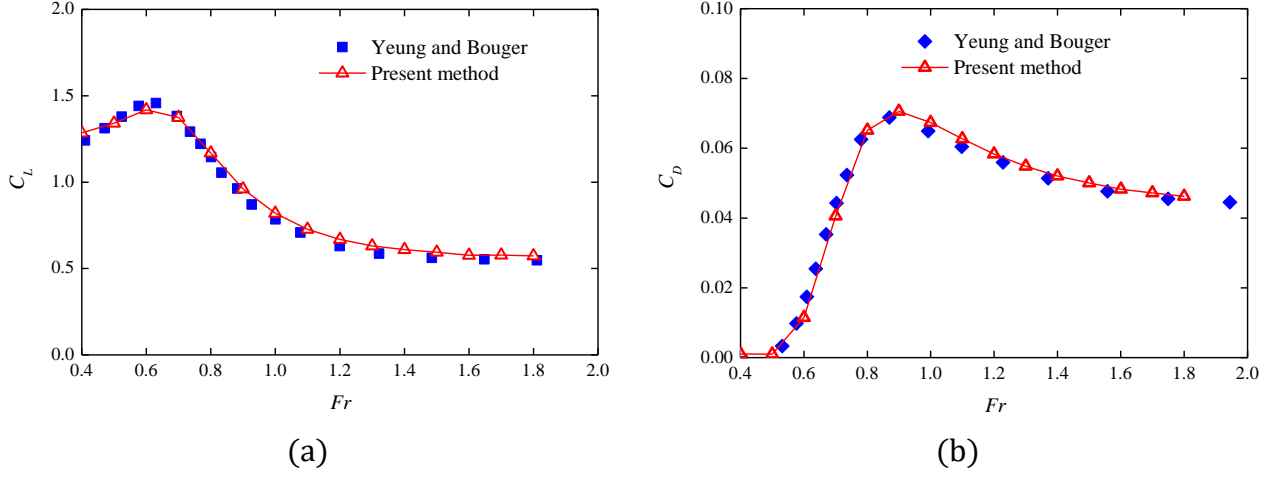
Fig. 21. Lift and drag versus the Froude number of a 2D NACA-4412 hydrofoil steadily operating beneath a free surface at $h/c = 1.0$, $d/c = 4.0$ and $\alpha = 5°$. (a) Lift coefficient; (b) Drag coefficient. $C_L = L/0.5\rho U^2 c$. $C_L =$ lift coefficient. $L =$ lift force. $C_D = D/0.5\rho U^2 c$. $C_D =$ drag coefficient. $D =$ drag force. $\rho =$ mass density of liquid. $U =$ ambient flow velocity. $c =$ chord length. $Fr = U/\sqrt{gc}$. $Fr =$ Froude number. $g =$ gravitational acceleration. $h =$ submergence depth of the hydrofoil. $d =$ water depth. $\alpha =$ angle of attack.

Fig. 21 presents the lift and drag coefficients for a 2D NACA-4412 hydrofoil as a function of the Froude number $Fr = U/\sqrt{gc}$. The horizontal length of the computational domain is 21 times the chord length, with the leading edge of the hydrofoil $5c$ from the upstream side. In addition, the length of the wake is 10 times the hydrofoil's chord length. The validity of the present study is examined against the numerical results obtained by Yeung and Bouger [31]. Here, 60 elements are distributed over each side of the hydrofoil. To be consistent with the work by Yeung and Bouger [31], the angle of attack is $\alpha = 5°$, the ratio between the submergence depth and the chord length is $h/c = 1.0$, and the water depth-to-chord length ratio is $d/c = 4.0$. We use both direct pressure integration (DPI) and conservation of fluid momentum (CFM) to calculate the hydrodynamic force, and the results obtained from both methods agree with one another. As illustrated in Fig. 21 (a), the lift coefficient varies strongly when the Froude number is greater than 0.4 but smaller than 1.0, which is observed as an initial increase followed by a decrease. Moreover, a peak value exists when the Froude number is equal to approximately 0.6. As depicted in Fig. 21 (b), when the Froude number is greater than 0.4, the drag coefficient increases considerably and reaches its maximum value when the Froude number is approximately 0.9. Then, the drag coefficient decreases with the Froude number. The agreement with the results by Yeung and Bouger [31] is reasonably satisfactory.

Then, the free-surface elevation induced by the steadily translating NACA-4412 hydrofoil is investigated at $h/c = 1.0$, $d/c = 4.0$ and $\alpha = 5°$ for various Froude numbers in Fig. 22. The position of the hydrofoil is within the interval $[-0.5, 0.5]$. Satisfactory agreement with the results calculated by Yeung and Bouger [31] is obtained.
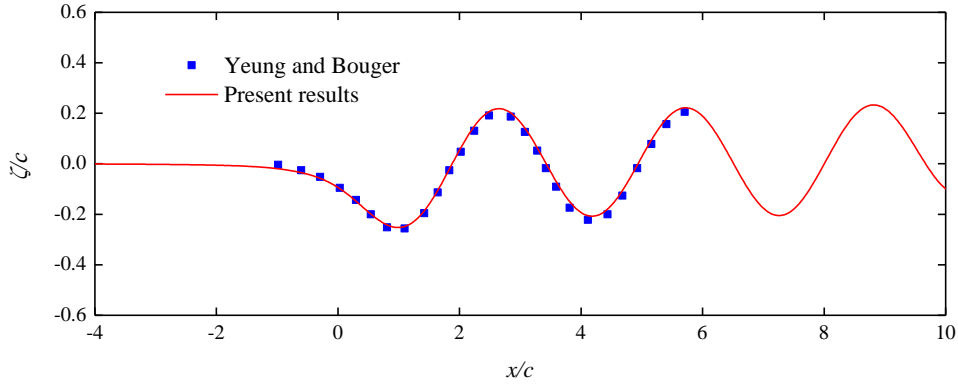
(a)
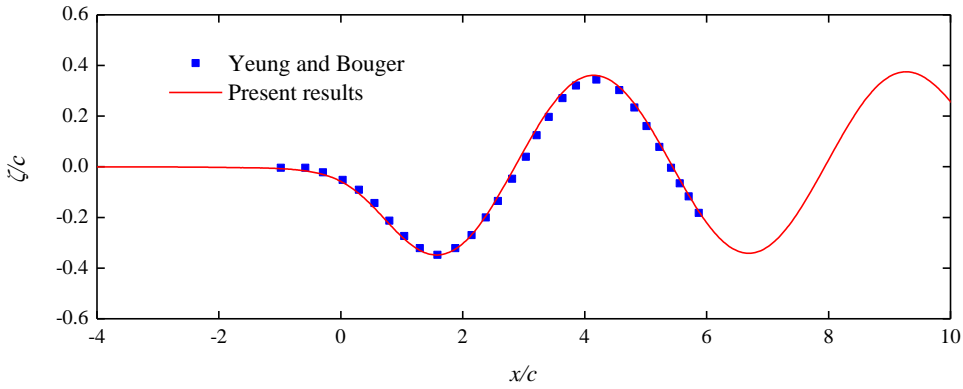
(b)

Fig. 22. Free-surface elevation generated by the NACA-4412 hydrofoil at $h/c = 1.0$, $d/c = 4.0$ and $\alpha = 5°$ compared with the numerical results by Yeung and Bouger [31]. (a) $Fr = 0.7$; (b) $Fr = 0.9$. $Fr = U/\sqrt{gc}$. $\zeta =$ Free-surface elevation. $x =$ horizontal position. $c =$ chord length. $x/c = -0.5$ is the leading edge and $x/c = 0.5$ is the trailing edge. $Fr =$ Froude number. $g =$ gravitational acceleration. $h =$ submergence depth of the hydrofoil. $d =$ water depth. $\alpha =$ angle of attack.

Finally, the calculated pressure coefficient, $C_P = (p - p_a)/(0.5\rho U^2)$, with p_a as the ambient pressure, is presented in Fig. 23 with the surface of the NACA-4412 hydrofoil at $\alpha = 5°$ and $Fr = 1.03$ for two submergence depths. In addition, the present results are verified and validated by comparing them with the numerical results reported by Giesing and Smith [13] and the experimental data reported by Ausman [3]. Furthermore, Giesing and Smith [13] assume a 2D linearized potential flow and apply a BEM. This study is more consistent with the numerical results reported by Giesing and Smith [13] than with the experimental results. In addition, the disagreement mainly occurs with respect to the suction side of the hydrofoil.
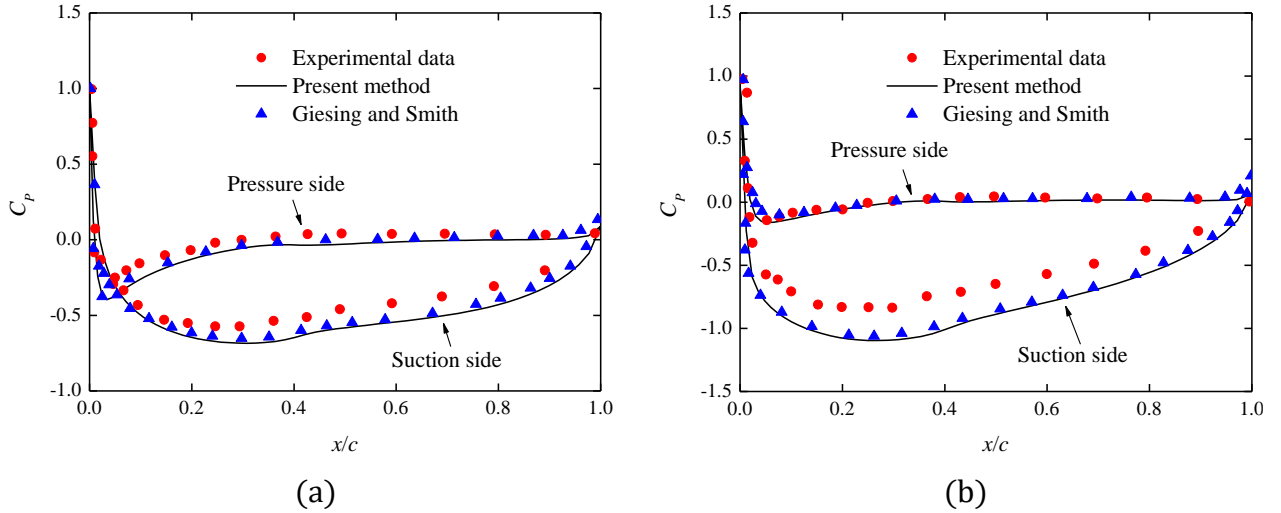
Fig. 23. Pressure distribution over a NACA-4412 hydrofoil at $\alpha = 5°$ and $Fr = 1.03$ for different submergences. (a) $h/c = 0.6$; (b) $h/c = 0.94$. $C_P = (p - p_a)/(0.5\rho U^2)$. $C_P =$ pressure coefficient. $p =$ pressure on the hydrofoil. $p_a =$ ambient pressure. $\rho =$ mass density of liquid. $U =$ ambient flow velocity. $Fr = U/\sqrt{gc}$. $Fr =$ Froude number. $g =$ gravitational acceleration. $c =$ chord length. $h =$ submergence depth. $\alpha =$ attack angle.

6 Conclusions and future studies

In this paper, two algorithms are proposed within the framework of the 2D HPC method [22] to treat singular flows and lifting problems in marine hydrodynamics. To reduce the required computational effort, the domain decomposition strategy is applied by representing far-field waves using eigen-function expansions [30, 31].

First, a domain decomposition strategy coupling the local solution in the inner region enclosing a sharp corner and the HPC method in the outer domain is proposed to investigate fluid-structure interaction problems in the presence of sharp corners and potential flow. For the added mass and damping associated with the linear hydrodynamic force, the results accounting for the singularity at the sharp corner do not differ much from those obtained using the conventional approach because the linear hydrodynamic force is only related to the velocity potential over the mean wetted surface of the body. At the sharp corner, the velocity potential is finite but the velocity components are singular. Thus, we study the second-order mean vertical force of a heaving rectangular cylinder, which is partly associated with the quadratic terms of the velocities in Bernoulli's equation. If the singularity at the sharp corner is accounted for, the results obtained from direct pressure integration (DPI) are consistent with those obtained from conservation of fluid momentum (CFM). Otherwise, a clear difference between the results from DPI and CFM is observed. However, neglecting the effect of the velocity singularity and using CFM produces results similar to those obtained by accounting for the flow singularity at sharp corners.

Then, the double-layer nodes algorithm is developed to model the velocity potential jump across a thin free shear layer shed from lifting bodies and the pressure difference across a flat

plate with a thickness of zero. By studying the steady lifting problem involving a flat plate with zero thickness, we concluded that the local solution can model the singularity at the leading edge and that the conventional HPC method can only yield a finite value at the leading edge. In addition, the transient unsteady and steady state lifting problem for a flat foil in infinite fluid and the steady lifting problem for a hydrofoil in the presence of a free surface were analyzed. The present numerical results obtained from the HPC method using the double-layer nodes technique are consistent with the analytical solutions and numerical results presented in the literature.

In summary, two novel algorithms within the framework of the 2D HPC method are developed to investigate singular flows and discontinuous problems in marine potential flow hydrodynamics. It has been verified that the proposed methods are valid and robust.

In future studies, the present algorithms will be extended to 3D problems. Furthermore, for fluid-structure interaction problems with sharp corners, the flow separation associated with the viscous effect will be examined. Therefore, the HPC method should be combined with a Navier-Stokes solver by solving the Navier-Stokes equations in the region where the viscous effect is predominant.

Acknowledgements

Appendix A. Computation of the integral in Eq. (25)

In Eq. (25), the integrand is oscillatory due to the presence of the trigonometric and Hankel functions. During the numerical integration, we first identify the truncation value of k. When k is large, we use the approximate asymptotic expression of the Hankel function, which is expressed as follows [1]:

$$\mathrm{H}_n^{(2)}(k) \approx \sqrt{\frac{2}{\pi k}} \exp\left[-\mathrm{i}\left(k - \frac{1}{2}n\pi - \frac{1}{4}\pi\right)\right].$$

(A.1)

Thus, the corresponding function $F(k)$ is simplified as follows:

$$F(k) = \Re\left[\frac{\mathrm{H}_1^{(2)}(k)}{\mathrm{H}_1^{(2)}(k) + \mathrm{i}\mathrm{H}_0^{(2)}(k)}\right] \approx \frac{1}{2},$$

(A.2)

which indicates that $F(k)$ is constant as k becomes infinitely large. Therefore, the upper limit of the integral k_U can be selected as the value at which $F(k)$ is near 0.5. Here, we set $k_U = 1000.0$, and the corresponding value of $F(k_U)$ is 0.5000000625, with a relative difference of

$O(10^{-7})$. When k is greater than k_U, we assume that $F(k)$ remains unchanged. Next, we find the zeroes of the integrand and numerically integrate between the adjacent zeroes. When ks is less than 0.1, we can use a Taylor expansion for the sine function, to obtain the following integral:

$$I_{0.1} = \frac{2}{\pi} \int_{0}^{0.1/s} \frac{F(k)}{k} \left[ks - \frac{1}{6}(ks)^3 + \frac{1}{120}(ks)^5 \right] dk$$

$$= \frac{2}{\pi} \int_{0}^{0.1/s} F(k) \left(s - \frac{1}{6}k^2 s^3 + \frac{1}{120}k^4 s^5 \right) dk. \tag{A.3}$$

Otherwise, the interval between the adjacent zeroes is divided into a number of subintervals, and the quadratic polynomial $a_0 + a_1 k + a_2 k^2$ is used to approximate the function $F(k)$ in each subinterval. Therefore, the elementary integral over each subinterval can be expressed as follows:

$$I = \frac{2}{\pi} \int_{k_1}^{k_2} \frac{F(k)}{k} \sin(ks) dk$$

$$= \frac{2}{\pi} \int_{k_1}^{k_2} \frac{a_0 + a_1 k + a_2 k^2}{k} \sin(ks) dk \tag{A.4}$$

$$= \frac{2}{\pi} \left[a_0 \mathrm{Si}(sk) - a_1 \frac{\cos ks}{s} + a_2 \frac{\sin(ks) - ks\cos(ks)}{s^2} \right]_{k_1}^{k_2},$$

where k_1 and k_2 are the minimum and maximum values of the subinterval and $\mathrm{Si}(\cdot)$ denotes the sine integral function [1].

Finally, the integral from the truncated value k_U to infinity is

$$I_{\infty} = \frac{2}{\pi} \int_{k_U}^{\infty} \frac{F(k)}{k} \sin(ks) dk$$

$$= \frac{1}{\pi} \int_{k_U}^{\infty} \frac{1}{k} \sin(ks) dk \tag{A.5}$$

$$= \frac{1}{\pi} \left[\frac{\pi}{2} - \mathrm{Si}(k_U s) \right].$$

Appendix B. Numerical calculation of the principle value integral in Eq. (36)

Herein, we demonstrate how to evaluate the principle value integral in Eq. (36), which takes the following form:

$$I = -\frac{\Gamma}{\pi} \mathrm{PV} \int_{0}^{\infty} \frac{k+\nu}{k} e^{-kh} \frac{\sinh k(y_V + h)\cosh k(y+h)}{\nu \sinh kh - k\cosh kh} \sin k(x - x_V) dk. \tag{B.1}$$

Converting Eq. (B.1) to the complex plane results in

$$I = \Im\left[-\frac{\Gamma}{\pi}\mathrm{PV}\int_0^\infty \frac{k+\nu}{k}\mathrm{e}^{-kh}\frac{\sinh k\left(y_V+h\right)\cosh k\left(y+h\right)}{\nu\sinh kh - k\cosh kh}\mathrm{e}^{ik\left(x-x_V\right)}\,dk\right]. \tag{B.2}$$

By expanding the hyperbolic sine and cosine functions in Eq. (B.2), we obtain

$$I = \Im\left[\frac{\Gamma}{2\pi}\mathrm{PV}\int_0^\infty \frac{k+\nu}{k}\frac{\mathrm{e}^{k\left(y+y_V\right)}+\mathrm{e}^{k\left(y_V-y-2h\right)}-\mathrm{e}^{k\left(y-y_V-2h\right)}-\mathrm{e}^{-k\left(y+y_V+4h\right)}}{\left(k-\nu\right)+\left(k+\nu\right)\mathrm{e}^{-2kh}}\mathrm{e}^{ik\left(x-x_V\right)}\,dk\right]. \tag{B.3}$$

Eq. (B.3) can be decomposed into four parts, each of which can be expressed as

$$I^* = \Im\left[\frac{\Gamma}{2\pi}\mathrm{PV}\int_0^\infty \frac{k+\nu}{k}\frac{\mathrm{e}^{-kY+ik\left(x-x_V\right)}}{\left(k-\nu\right)+\left(k+\nu\right)\mathrm{e}^{-2kh}}\,dk\right], \tag{B.4}$$

where Y is always greater than zero. Following the study conducted by An and Faltinsen [2], we introduce the two following functions:

$$T(k) = \frac{k+\nu}{k} \quad \text{and} \quad Q(k) = \left(k-\nu\right)+\left(k+\nu\right)\mathrm{e}^{-2kh}. \tag{B.5}$$

Then, we generate the Taylor expansion of $Q(k)$ at k_0 as follows:

$$Q(k) = Q(k_0)+Q'(k_0)\cdot(k-k_0)+\ldots, \tag{B.6}$$

with $Q(k_0) = 0$. When considering Eq. (B.5) and Eq. (B.6), Eq. (B.4) can be rewritten as follows:

$$I^* = \Im\left\{\frac{\Gamma}{2\pi}\mathrm{PV}\int_0^\infty \left[\frac{T(k)}{Q(k)}-\frac{T(k_0)}{(k-k_0)Q'(k_0)}\right]\mathrm{e}^{-kY+ik\left(x-x_V\right)}\,dk + \frac{\Gamma}{2\pi}\frac{T(k_0)}{Q'(k_0)}\mathrm{PV}\int_0^\infty \frac{\mathrm{e}^{-kY+ik\left(x-x_V\right)}}{k-k_0}\,dk\right\}. \tag{B.7}$$

In Eq. (B.7), the first integral is not singular but the second one is. Thus, our efforts are devoted to evaluating the second integral in Eq. (B.7). For the integration path demonstrated in Fig. B1, the second integral occurs along path L. C denotes the integration along the circular arc with radius ρ_C, and it can be verified that the integration along C vanishes as ρ_C tends towards infinity. In the complex $k-$plane, it is possible to find an argument Λ such that the exponential function is purely real; thus, the argument Λ can be expressed as follows:

$$\Lambda = \arctan\left(\frac{x-x_V}{Y}\right). \tag{B.8}$$

Because Y is greater than zero, the sign of the argument Λ depends on $x-x_V$. The integration along path $L_\pm$, where the exponential function is purely real, can be expressed as the exponential integral function as follows [1]:

34

$$\int_{L_\pm} \frac{e^{-kY+ik(x-x_V)}}{k-k_0} dk = e^{-k_0 Y+ik_0(x-x_V)} E_1\left[-k_0 Y + i k_0 (x-x_V)\right]. \tag{B.9}$$

For Λ values greater than zero, the integration path is as shown in the left panel of Fig. B1 and

$$\int_L + \int_{L_\varepsilon} - \int_C - \int_{L_+} = 2\pi i Res(k_0). \tag{B.10}$$
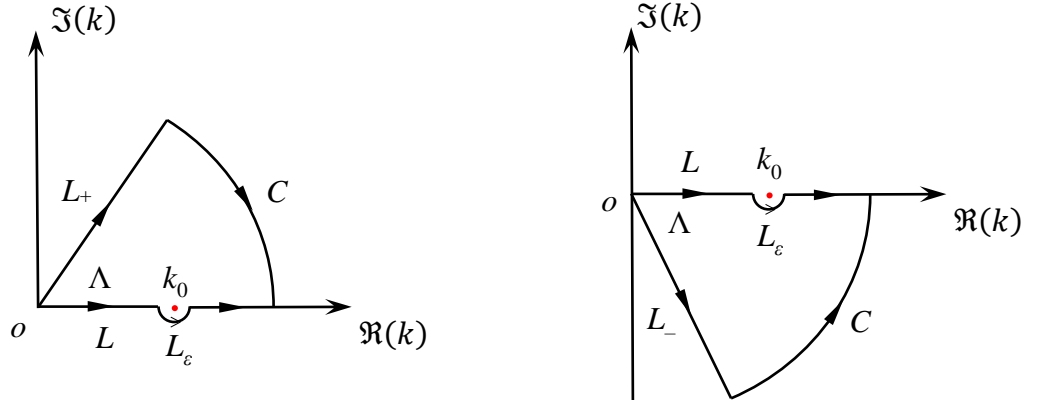

Fig. B1. Integration path in the complex $k-$plane.

When Λ is less than zero, the integration path is as shown in the right panel of Fig. B1 and the integration path is

$$\int_L + \int_{L_\varepsilon} - \int_C - \int_{L_-} = 0. \tag{B.11}$$

with

$$\int_{L_\varepsilon} \frac{e^{-kY+ik(x-x_V)}}{k-k_0} dk = \pi i\, e^{-k_0 Y+ik_0(x-x_V)}. \tag{B.12}$$

Therefore, the second integral in Eq. (B.7) is simplified as follows:

$$PV\int_0^\infty \frac{e^{-kY+ik(x-x_V)}}{k-k_0} dk = \begin{cases} e^{-k_0 Y+ik_0(x-x_V)} E_1\left[-k_0 Y + i k_0 (x-x_V)\right] + \pi i\, e^{-k_0 Y+ik_0(x-x_V)} & \text{as } \Lambda > 0, \\ e^{-k_0 Y+ik_0(x-x_V)} E_1\left[-k_0 Y + i k_0 (x-x_V)\right] - \pi i\, e^{-k_0 Y+ik_0(x-x_V)} & \text{as } \Lambda < 0. \end{cases} \tag{B.13}$$

Finally, the principle integral in Eq. (B.1) can be evaluated accurately and efficiently.

References

1   Abramowitz M, Stegun I. Handbook of Mathematical Functions with Formulas, Graphs and Mathematical Tables. Dover Publications Inc, New York, 1964.

2   An S, Faltinsen OM. Linear free-surface effects on a horizontally submerged and perforated 2D thin plate in finite and infinite water depths. Appl Ocean Res 2012; 37: 220-234.

3   Ausman JS. Pressure limitation on the upper surface of a hydrofoil. University of California, Berkeley, USA, 1954.

4   Baarholm R. Theoretical and experimental studies of wave impact underneath decks of offshore platforms. Norwegian University of Science and Technology, Trondheim, Norway, 2001.

5   Bingham HB, Zhang H. On the accuracy of finite difference solutions for nonlinear water waves. J Eng Math 2007; 58: 211-228.

6   Bisplinghoff RL, Ashley H, Halfman RL. Aeroelasticity. Dover Publications, New York, 1996.

7   Chen XB. Middle-field formulation for the computation of wave-drift loads. J Eng Math 2007; 59: 61–82.

8   Dommermuth DG, Yue DKP, Lin WM, Rapp RJ, Chan ES, Melville WK. Deep-water plunging breakers: a comparison between potential theory and experiments. J Fluid Mech 1988; 189: 423-442.

9   Faltinsen OM. Sea Loads on Ships and Offshore Structures. Cambridge University Press, Cambridge, 1993.

10   Faltinsen OM. Hydrodynamics of High-Speed Marine Vehicles. Cambridge University Press, New York, 2005.

11   Faltinsen OM, Timokha AN. Analytically approximate natural sloshing modes and frequencies in two-dimensional tanks. Eur J Mech B-Fluid 2014; 47: 176-187.

12   Fredriksen AG, Kristiansen T, Faltinsen OM. Experimental and numerical investigation of wave resonance in moonpools at low forward speed. Appl Ocean Res 2014; 47: 28-46.

13   Giesing JP, Smith AMO. Potential flow about two-dimensional hydrofoils. J Fluid Mech 1967; 28: 113-129.

14   Greco M, Colicchio G, Faltinsen OM. A domain-decomposition strategy for a compressible multi-phase flow interacting with a structure. Int J Numer Meth Eng 2014; 98: 840-858.

15   Greengard LF, Rokhlin V. A fast algorithm for particle simulations. J Comput Phys 1987; 73: 325-348.

16   Lee CH. On the evaluation of quadratic forces on stationary bodies. J Eng Math 2007; 58: 141-148.

17   Mavrakos SA. The vertical drift force and pitch moment on axisymmetric bodies in regular waves. Appl Ocean Res 1988; 10: 207-218.

18   Nakos D, Sclavounos PD. On steady and unsteady ship wave patterns. J Fluid Mech 1990; 215: 263-288.

19   Newman JN. Marine Hydrodynamics. The MIT Press, Cambridge, Massachusetts, 1977.

20 Nestegard A, Sclavounos PD. A numerical solution of two-dimensional deep water wave-body problems. J Ship Res 1984; 28: 48-54.

21 Rokhlin V. Rapid solution of integral equations of classical potential theory. J Comput Phys 1985; 60: 187-207.

22 Shao YL, Faltinsen OM. Towards efficient fully-nonlinear potential-flow solvers in marine hydrodynamics. in: Proc. of the 31st Int Conf on Ocean, Offshore and Arc Eng (OMAE), Rio de Janeiro, Brazil, 2012.

23 Shao YL, Faltinsen OM. A harmonic polynomial cell (HPC) method for 3D Laplace equation with application in marine hydrodynamics. J Comput Phys 2014; 274: 312-332.

24 Ursell F. On the heaving motion of a circular cylinder on the surface of a fluid. Q J Mech Appl Math 1949; 2: 218-231.

25 Vugts J. The hydrodynamic coefficients for swaying, heaving and rolling cylinders in a free surface. Netherlands Ship Research Centre Report, 1968, No. 112S.

26 Wehausen JV, Laitone EV. Surface waves. Handbuch der Physik. Heidelberg, Springer-Verlag, 1960.

27 Wu GX, Eatock Taylor R. Time stepping solutions of the two-dimensional nonlinear wave radiation problem. Ocean Eng 1995; 22: 785-798.

28 Xue M, Xu H, Liu Y, Yue DKP. Computations of fully nonlinear three-dimensional wave-wave and wave-body interactions. Part 1. Dynamics of steep three-dimensional waves. J Fluid Mech 2001; 438: 11-39.

29 Yan H, Liu Y. An efficient high-order boundary element method for nonlinear wave-wave and wave-body interactions. J Comput Phys 2011; 230: 402-424.

30 Yeung RW. A hybrid integral-equation method for time-harmonic free-surface flow. The First Int Conf on Num Ship Hydrodyn, Gaithersburg, German, 1975 pp. 581-607.

31 Yeung RW, Bouger YC. A hybrid integral-equation method for steady two-dimensional ship waves. Int J Numer Meth Eng 1979; 14: 317-336.

32 Zhao R, Faltinsen OM. Interaction between current, waves and marine structures. in: Proc of the 5th Int Conf on Num Ship Hydrodyn, Hiroshima, Japan, 1989 pp. 513-527.